Article

Neuron

Modulating Neuronal Competition Dynamics in the Dentate Gyrus to Rejuvenate Aging Memory Circuits

Highlights

- Mature DGC spine elimination enhances integration of adult-born DGCs
- Adult neurogenesis dictates population-based coding in the DG
- Integration of adult-born DGCs transiently reorganizes local afferent connectivity
- Rejuvenating the aged DG with adult-born DGCs promotes memory precision

Authors

Kathleen M. McAvoy, Kimberly N. Scobie, Stefan Berger, ..., Rene Hen, Benedikt Berninger, Amar Sahay

Correspondence

asahay@mgh.harvard.edu

In Brief

McAvoy et al. demonstrate that neuronal competition dictates integration of adult-born dentate granule neurons. By biasing competition in favor of adult-born neurons in adulthood and aging, McAvoy et al. rejuvenate the dentate gyrus with new neurons and improve remapping and memory.

McAvoy et al., 2016, Neuron *91*, 1–18
September 21, 2016
http://dx.doi.org/10.1016/j.neuron.2016.08.009

CellPress

Please cite this article in press as: McAvoy et al., Modulating Neuronal Competition Dynamics in the Dentate Gyrus to Rejuvenate Aging Memory Circuits, Neuron (2016), http://dx.doi.org/10.1016/j.neuron.2016.08.009

Neuron
Article

Modulating Neuronal Competition Dynamics in the Dentate Gyrus to Rejuvenate Aging Memory Circuits

Kathleen M. McAvoy,[1,2,3] Kimberly N. Scobie,[4] Stefan Berger,[5] Craig Russo,[1,2] Nannan Guo,[1,2,3] Pakanat Decharatanachart,[1] Hugo Vega-Ramirez,[1,2,3] Sam Miake-Lye,[1] Michael Whalen,[6] Mark Nelson,[7] Matteo Bergami,[8] Dusan Bartsch,[5] Rene Hen,[4] Benedikt Berninger,[9] and Amar Sahay[1,2,3,10,11,*]

[1]Center for Regenerative Medicine, Massachusetts General Hospital, Boston, MA 02114, USA
[2]Harvard Stem Cell Institute, Cambridge, MA 02138, USA
[3]Department of Psychiatry, Massachusetts General Hospital, Harvard Medical School, Boston, MA 02114 USA
[4]Departments of Neuroscience and Psychiatry, Columbia University, New York, NY 10032, USA
[5]Department of Molecular Biology, Central Institute of Mental Health and Medical Faculty Mannheim, Heidelberg University, 68159 Mannheim, Germany
[6]Neuroscience Center, Massachusetts General Hospital, Boston, MA 02129, USA
[7]Echelon Biosciences, Salt Lake City, UT 84108, USA
[8]Cologne Excellence Cluster on Cellular Stress Responses in Aging-Associated Diseases (CECAD) and University Hospital of Cologne, Joseph-Stelzmann-Straße 26, D-50931 Cologne, Germany
[9]Institute of Physiological Chemistry, University Medical Center Johannes Gutenberg University, 55128 Mainz, Germany
[10]Broad Institute of Harvard and MIT, Cambridge, MA 02142, USA
[11]Lead Contact
*Correspondence: asahay@mgh.harvard.edu
http://dx.doi.org/10.1016/j.neuron.2016.08.009

SUMMARY

The neural circuit mechanisms underlying the integration and functions of adult-born dentate granule cell (DGCs) are poorly understood. Adult-born DGCs are thought to compete with mature DGCs for inputs to integrate. Transient genetic overexpression of a negative regulator of dendritic spines, Kruppel-like factor 9 (Klf9), in mature DGCs enhanced integration of adult-born DGCs and increased NSC activation. Reversal of *Klf9* overexpression in mature DGCs restored spines and activity and reset neuronal competition dynamics and NSC activation, leaving the DG modified by a functionally integrated, expanded cohort of age-matched adult-born DGCs. Spine elimination by inducible deletion of Rac1 in mature DGCs increased survival of adult-born DGCs without affecting proliferation or DGC activity. Enhanced integration of adult-born DGCs transiently reorganized adult-born DGC local afferent connectivity and promoted global remapping in the DG. Rejuvenation of the DG by enhancing integration of adult-born DGCs in adulthood, middle age, and aging enhanced memory precision.

INTRODUCTION

Neural stem cells (NSCs) in the dentate gyrus (DG) sub-region of the hippocampus generate dentate granule cells (DGCs) throughout life, with substantial turnover of the DG reported in humans (Altman and Das, 1965; Eriksson et al., 1998; Spalding et al., 2013). Considerable evidence suggests that levels of adult hippocampal neurogenesis are highly sensitive to experience (Kempermann et al., 1997; van Praag et al., 2000), indicating that neurogenesis is dynamically regulated by circuit demands. It has been suggested that adult-born DGCs must compete with mature DGCs for entorhinal cortical inputs in order to integrate into the hippocampal circuit. Anatomical studies show that maturing adult-born DGCs first form synapses onto pre-existing perforant path-DGC synapses, before establishing monosynaptic connections with those perforant path terminals (Toni et al., 2007). Deletion of the N-Methyl-D-aspartate (NMDA) receptor in 2- to 3-week-old adult-born DGCs impairs their survival, indicating a role for activity in integration of adult-born DGCs (Tashiro et al., 2006). These observations raise the possibility that mature DGC input connectivity dictates the dynamics of adult-born DGC competition.

Studies interrogating functional contributions of adult hippocampal neurogenesis support a role for adult-born DGCs in resolving interference between competing goals or overlapping contextual or spatial information (Wojtowicz et al., 2008; Clelland et al., 2009; Garthe et al., 2009; Tronel et al., 2012; Sahay et al., 2011a; Burghardt et al., 2012; Nakashiba et al., 2012; Niibori et al., 2012; Pan et al., 2012; Vukovic et al., 2013; Swan et al., 2014; Besnard and Sahay, 2016). Aging is accompanied by numerous changes in the hippocampus associated with impairments in resolution of interference (Toner et al., 2009; Yassa et al., 2011; Yassa and Stark, 2011; Gracian et al., 2013; Wu et al., 2015). Whether enhancing adult hippocampal neurogenesis in middle age or during aging improves memory functions is not known.

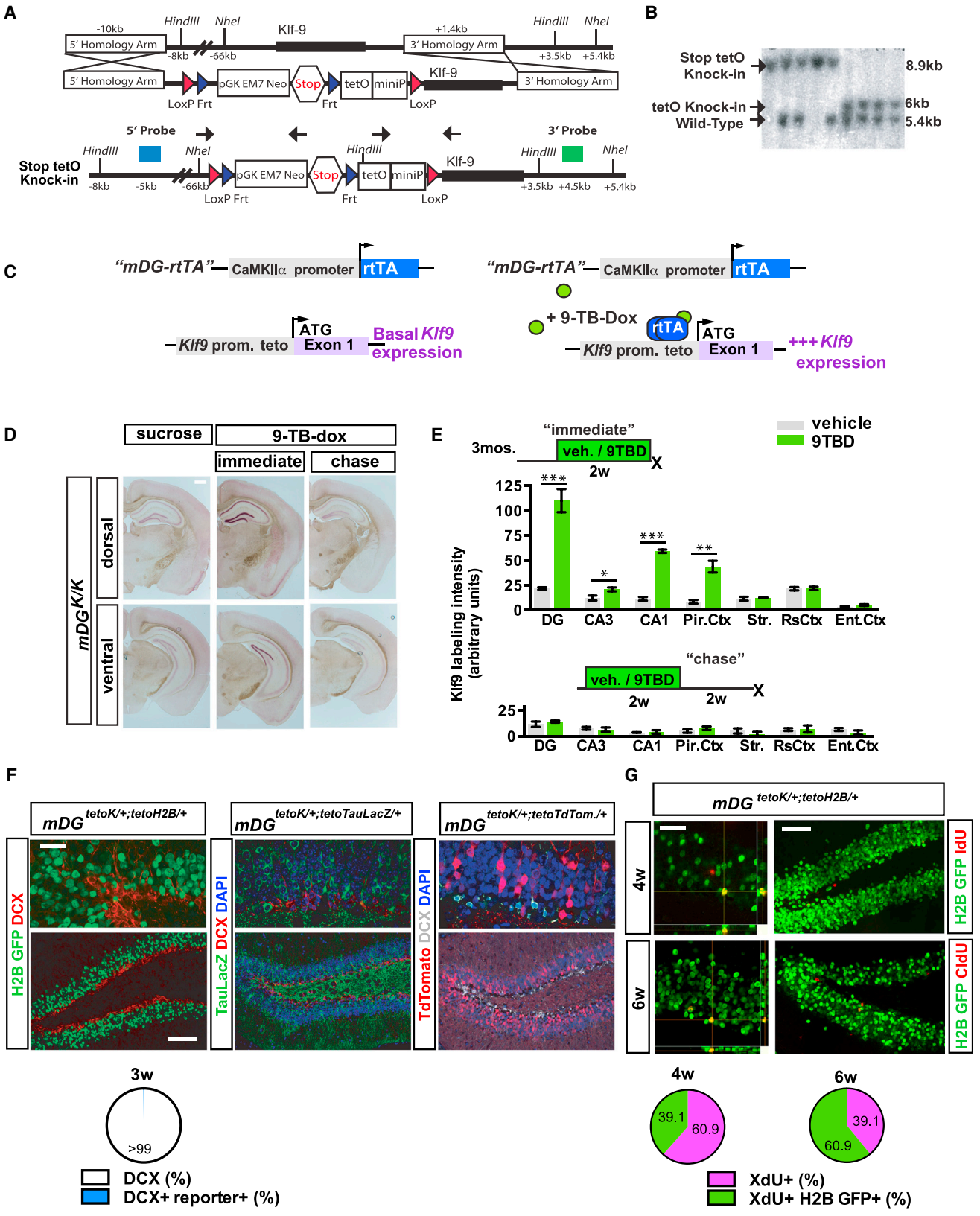

(legend on next page)

One neural mechanism by which interference between similar memories in the DG-CA3 circuit is decreased is through pattern separation, a process by which similar inputs are made more distinct during storage (McNaughton and Morris, 1987; O'Reilly and McClelland, 1994; Gilbert et al., 2001; Rolls and Kesner, 2006; Bakker et al., 2008). In the DG, this computational process may be mediated by encoding inputs in non-overlapping ensembles of neurons (global remapping) (Leutgeb et al., 2007; Deng et al., 2013; Neunuebel and Knierim, 2014). Whether adult neurogenesis promotes network-level mechanisms underlying pattern separation in the DG is not known.

To begin to bridge these gaps in our understanding, we engineered a genetic system to inducibly and reversibly overexpress a negative transcriptional regulator of dendritic spines, Kruppel-like factor 9 (Klf9), in mature DGCs. *Klf9* overexpression eliminated a subset of dendritic spines of mature DGCs, decreased their activity, and robustly enhanced integration of adult-born DGCs and activation of NSCs without affecting olfactory bulb neurogenesis. Independently targeting *Rac1* to eliminate spines in mature DGCs likewise promoted the integration of adult-born DGCs. Restoration of *Klf9* expression to physiological levels restored dendritic spines and reverted levels of neurogenesis to steady state, while modifying the DG with an integrated, expanded population of adult-born DGCs. Adult mice with an expanded cohort of 5- to 8-week-old adult-born DGCs showed improved cognitive flexibility, memory precision, and long-term contextual memory, whereas rejuvenating the DG during aging improved memory precision. Expanding the population of 5- to 8-week-old adult-born DGCs enhanced global remapping in the DG, causally linking adult hippocampal neurogenesis with network-level mechanisms supporting pattern separation in the DG.

RESULTS

A Genetic System for Inducible and Reversible Overexpression of *Klf9* in Mature DGCs

To determine the impact of modulating dendritic spines of mature DGCs on neuronal competition dynamics and NSC activation, we developed a genetic system to reversibly eliminate dendritic spines of mature DGCs in the adult hippocampus. As previous work suggests that Klf9 functions as a negative regulator of dendritic spines of hippocampal neurons in vitro and in vivo (Scobie et al., 2009) (K.N.S. and A.S., unpublished data), without affecting neuronal survival, we hypothesized that *Klf9* overexpression in mature DGCs would decrease their dendritic spine density. We generated a tetO-Klf9 knockin mouse line to permit reversible induction of *Klf9* expression in vivo. tetO-Klf9 knockin mice exhibit comparable *Klf9* expression to wild-type mice (data not shown) and were bred with a CaMKIIα rtTA driver sub-line to generate bigenic CaMKIIα rtTA; tetO-Klf9/tetO-Klf9 mice (hereafter $mDG^{K/K}$ mice) (Figures 1A–1C). We selected this CaMKIIα rtTA driver line based on robust induction of three independent tetO-linked transgenes in mature, but not immature, Doublecortin-positive (DCX+) DGCs ≤3 weeks of age (Snyder et al., 2009), by 2 weeks of 9-tert-butyl-doxycycline (9TBD) treatment (Figures 1F–1G; Figures S1C–S1F). Further, we found using a tetO-H2B GFP reporter line (Foudi et al., 2009) that rtTA transactivates H2B-GFP expression in 39.13% ± 8.59% of 4-week-old adult-born cells and 60.86% ± 8.62% of 6-week-old adult-born cells. Adult $mDG^{K/K}$ mice showed significant elevation of levels of *Klf9* transcripts in the DG-GCL (but not hilar cells), CA3, CA1, and piriform cortex after 2 weeks of 9TBD treatment (Figures 1D and 1E; Figures S1A and S1B, t test, vehicle versus 9TBD, DG $p < 0.0001$, CA3 $p = 0.0152$, CA1 $p < 0.0001$, PC $p = 0.0004$). Critically, *Klf9* overexpression reverted to baseline levels following a 2-week-long "chase" period (Figures 1D and 1E; Figure S1B).

Reversible Overexpression of *Klf9* in Mature DGCs Transiently Decreases Their Dendritic Spine Density and Activity

To determine the effect of *Klf9* overexpression on dendritic spine density, we bred $mDG^{K/K}$ mice with Thy-1 GFP (M line) mice in which GFP is expressed in DGCs >6 weeks of age (Figures 2A and 2B) (Vuksic et al., 2008). Induction of *Klf9* overexpression in $mDG^{K/K;Thy\text{-}1GFP}$ mice decreased spine density in the outer molecular layer (OML) of the DG (t test, vehicle versus 9TBD, dorsal $p = 0.0074$, ventral $p = 0.0067$) and stratum radiatum (SR) of dorsal CA1 (t test, vehicle versus 9TBD, $p = 0.0264$) without affecting spine density in the inner molecular layer (IML) of the DG (Figures 2C–2D; Figure S2F, immediate time point). *Klf9* overexpression likely decreased functional spines, as $mDG^{K/K;Thy\text{-}1GFP}$ mice also showed a reduction in the density of PSD95-containing spines in the OML (t test, vehicle versus 9TBD, $p = 0.0095$) (Figure 2G); however, *Klf9* overexpression did not change the distribution of dendritic spine size in the DG or CA1 (Figures 2E and 2F) or size distribution of mossy fiber terminals of mature DGCs (Figure 2H). Reversal of *Klf9* overexpression restored spine density at the chase time point (Figures 2C and 2D). This restoration is unlikely to be due to homeostatic changes since 4 weeks of *Klf9* overexpression in $mDG^{K/K}$ mice maintained dendritic spine loss in the DG (Figure 3K, data not shown). Analysis of cleaved caspase-3+ cells in the GCL of vehicle- and 9TBD-treated $mDG^{K/K}$ mice detected negligible caspase activation, indicating that *Klf9* overexpression and the

Figure 1. A Genetic System for Inducible and Reversible Overexpression of *Klf9* in Mature DGCs

(A) Strategy for targeting *Klf9* locus to generate tetO-Klf9 knockin mouse line.

(B) Southern blot on F2 offspring DNA digested with *NheI* and probed with the 3′ probe showing all three alleles (WT, Stop tetO-Knock-in, and TetO-Knock-in).

(C–E) Inducible and reversible overexpression of *Klf9*. (C) Schematic of tet-on genetic system. (D) In situ hybridization shows *Klf9* transcripts in $mDG^{K/K}$ mice are increased following 2 weeks of 9TBD treatment in drinking water (immediate) and are restored after a 2-week chase period. (E) Quantification of (D) (arbitrary units) at the immediate (top, n = 5, 3) and chase (n = 3, 3; bottom) time point.

(F) The *mDG rtTA* line drives expression in DGCs older than 3 weeks of age. Confocal images show absence of DCX and teto-reporter overlap in DGCs.

(G) rtTA transactivates the *tetO-H2B GFP* transgene in DGCs 4 weeks of age and older (n = 3 mice). Scale bar represents 500 μm in (D), 20 μm in top of (F), 100 μm in bottom of (F), 20 μm in top of (G), and 75 μm in right of (G). Data are represented mean ± SEM. ***$p < 0.001$, **$p < 0.01$, *$p < 0.05$.

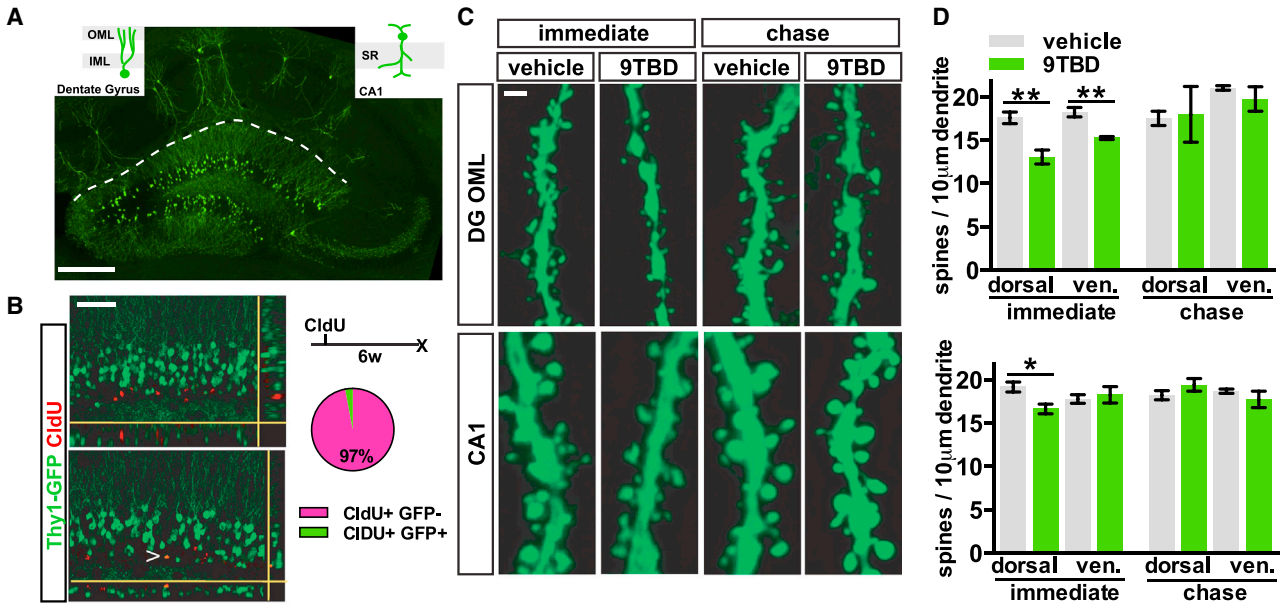

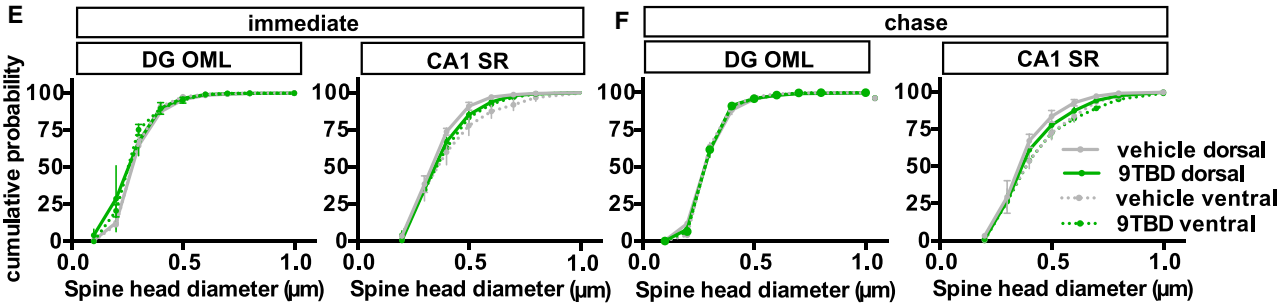

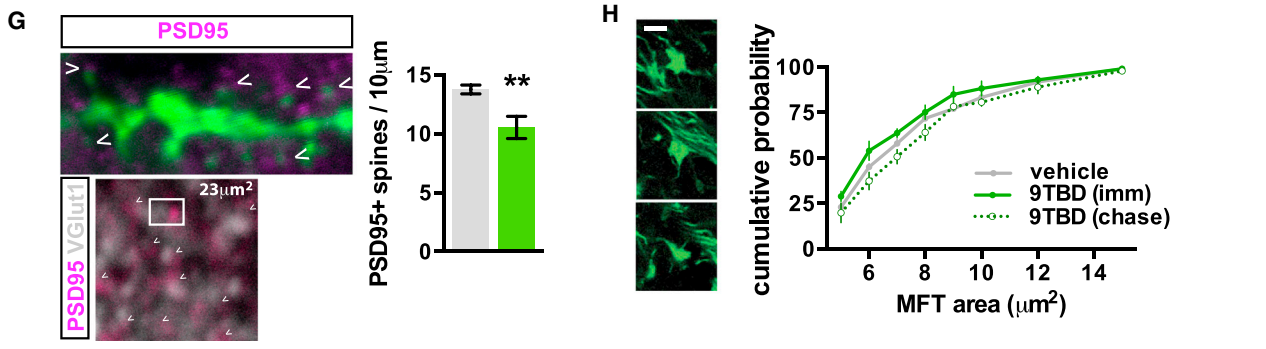

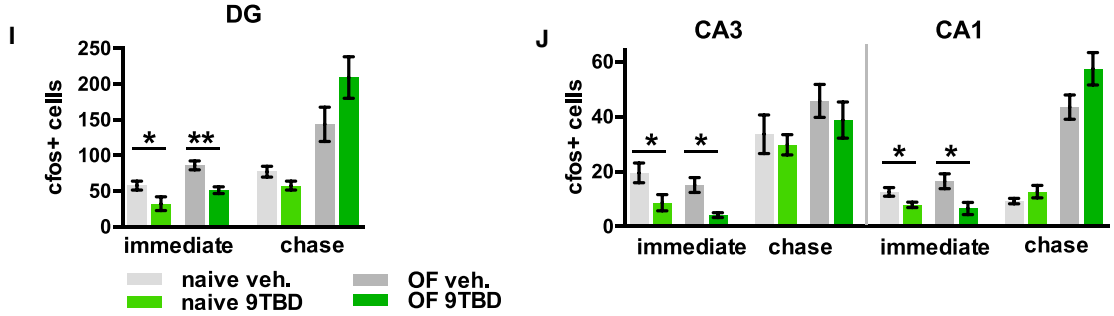

(legend on next page)

reduction in mature DGC spine density does not cause cell death (Figure S2H).

Klf9 overexpression (immediate time point) resulted in a significant decrease in activity of DG, CA3, and CA1 at baseline (home cage, t test, vehicle versus 9TBD, DG p = 0.0353, CA3 p = 0.0446, CA1 p = 0.0242) and following exploration of an open field (Figure 2I; Figures S2A and S2B) (t test, vehicle versus 9TBD, DG p = 0.0092, CA3 p = 0.0269, CA1 p = 0.0488). Reversal of *Klf9* overexpression (chase time point) restored neuronal activation (Figure 2J; Figures S2C and S2D) in parallel with the restoration of dendritic spine density in DG-OML and CA1-SR. 9TBD- and vehicle-treated $mDG^{K/K}$ mice also showed comparable spine densities of striatal and retrosplenial cortical neurons at the chase time point (Figures S2E and S2G). Thus, inducible *Klf9* overexpression negatively regulates dendritic spine density and activity of mature DGCs in vivo.

Reversible Overexpression of *Klf9* in Mature DGCs Modulates Neuronal Competition Dynamics and Activation of NSCs

We next addressed the impact of decreasing mature DGC dendritic spines and activity on neuronal competition dynamics and NSC activation. 9TBD-treated $mDG^{K/K}$ mice showed a 1.8- ± 0.07-fold increase (t test, vehicle versus 9TBD, p = 0.0028) in the DCX+ population at the immediate time point, and this enhancement in DCX+ numbers reverted back to steady-state levels at the chase time point (Figures 3A–3C). The enhancement in the DCX+ population was dependent on both genotype and treatment (Figure S3C) and limited to the DG, with no effect on SVZ neurogenesis (Figure S3E–S3G). Importantly, the transient enhancement in the DCX+ population translated into a 1.86- ± 0.19-fold increase (t test, vehicle versus 9TBD, p = 0.0118) in survival of mature (5-week-old) adult-born DGCs following restoration of *Klf9*, thereby modifying the DG with an expanded cohort of surviving age-matched adult-born DGCs (Figures 3A–3B and 3F; Figures S3A and S3B). Cell-fate specification in this surviving population (79.5% ± 5.1% NeuN+) was unaffected by *Klf9* overexpression in mature DGCs (Figures S4A and S4B).

To ascertain the age of adult-born DGCs whose survival was impacted by *Klf9* overexpression in mature DGCs, we labeled dividing cells at multiple time points prior to, and during, 9TBD treatment of $mDG^{K/K}$ mice (Figure S3A). We found that the survival of ~2- to 3-week-old, but not 3- to 4-week-old, adult-born cells was enhanced by *Klf9* overexpression in mature DGCs (Figures S3A, S3B, and S3D), consistent with previous reports suggesting a critical window for activity-dependent integration (Tashiro et al., 2006). In addition, the population of cells born 1 week into the course of 9TBD treatment was also expanded (data not shown). These data suggest that a 2 week induction-2 week chase protocol enables expansion of a cohort of 3- to 6-week-old adult-born DGCs.

To further probe the relationship between dendritic spines of mature DGCs and adult hippocampal neurogenesis, we analyzed the DCX+ population in $mDG^{K/K;Thy1\text{-}GFP}$ mice in which we quantified mature DGC spine density (Figures 2C and 2D). We found that the size of the DCX+ adult-born DGC population is inversely correlated with spine density of mature DGCs (vehicle: n = 9, Spearman $r = -0.6193$, p = 0.0497; 9TBD: n = 14, Spearman $r = -0.6879$, p = 0.0082, combined groups: Spearman $r = -0.7540$, $p < 0.0001$, Figure 3K).

Interestingly, *Klf9* overexpression in mature DGCs also increased activation of NSCs and progenitors (Figures 3A, 3B, 3D, 3E, and 3G–3J). At the immediate time point, 9TBD-treated $mDG^{K/K}$ mice exhibited significant increases in activation of NSCs and progenitors expressing mini-chromosome maintenance factor 2 (MCM2, a marker of cell cycle and G0 to early G1 transition, t test, vehicle versus 9TBD, IMM p = 0.0048) or Tbr2 (t test, vehicle versus 9TBD, p = 0.0023, Figures 3A and 3D–3E). We also saw a significant increase in activated type I NSCs (Nestin-expressing cells with radial-glial-like morphology that co-express MCM2, Figures 3G–3H, t test, vehicle versus 9TBD, p = 0.0001). In addition, we bred Nestin-GFP mice with $mDG^{K/K}$ mice and observed an increase in GFP+ type I cells that also expressed MCM2 (Figures 3I–3J, t test, vehicle versus 9TBD, p = 0.0219). Furthermore, the 3.37- ± 0.38-fold enhancement in NSC activation is transient and returns to basal levels following a 2-week chase (Figure 3H).

We next asked whether we could repeatedly enhance neurogenesis in $mDG^{K/K}$ mice. We found that a second treatment with 9TBD 56 days following the first induction induced *Klf9* overexpression, activation of NSCs, and expansion of the population of adult-born DGCs to similar extent as that seen following a single treatment of 9TBD (Figures S6F–S6L). Thus, $mDG^{K/K}$ mice can be used to modify the DG with expanded populations of age-matched adult-born DGCs over multiple time points in the animal's lifetime.

Figure 2. Reversible Overexpression of *Klf9* Transiently Decreases Dendritic Spine Density and Activity of Mature DGCs

(A) GFP is expressed in a subset of DGCs and CA1 pyramidal neurons in $mDG^{K/K;\ Thy1\text{-}GFP(M)/+}$ mice.

(B) GFP+ DGCs in $mDG^{K/K;\ Thy1\text{-}GF\ (M)/+}$ are 6 weeks of age or older. Confocal scans of the GCL showing 6-week-old DGCs (CldU+) expressing GFP (arrowhead indicates overlap, n = 3).

(C and D) Inducible *Klf9* overexpression decreases dendritic spine density. (C) Maximum intensity projection confocal images of individual dendritic segments from OML (top) and CA1-SR (bottom) at the immediate and chase time point in $mDG^{K/K;\ Thy1\text{-}GFP/+}$ mice. (D) Quantification of (C) (n = 4, 3).

(E and F) The distribution of spine head diameter is unchanged in OML or SR of $mDG^{K/K;\ Thy1\text{-}GFP/+}$ mice at the immediate (E) and chase (F) time points (n = 4, 3 immediate; n = 3, 3 chase).

(G) Inducible *Klf9* overexpression decreases the density of PSD95+ dendritic spines. Left, top: overlap between PSD95 and GFP-expressing dendrite. Left, bottom: representative image from DG OML showing adjacent opposing puncta of PSD95 and Vesicular glutamate transporter-1 (vGlut1). Right: quantification of PSD95+ dendritic spine density in the OML (n = 3, 5).

(H) *Klf9* overexpression in mature DGCs does not affect MFT size. Graph displays the percentage distribution of MFT area (n = 7 [vehicle], 4[immediate], 3[chase]).

(I and J) *Klf9* overexpression in mature DGCs transiently decreases the cfos+ population at the immediate time point (home cage [n = 7, 7], 30 min of open field exploration [n = 6, 3]) in DG (I) and CA3 and CA1 (J), but not the chase time point (home cage n = 6, 6, open field n = 3,3). Scale bar represents 500 μm in (A), 20 μm in (B), and 2 μm in (C), (G), and (H). Data are represented mean ± SEM.

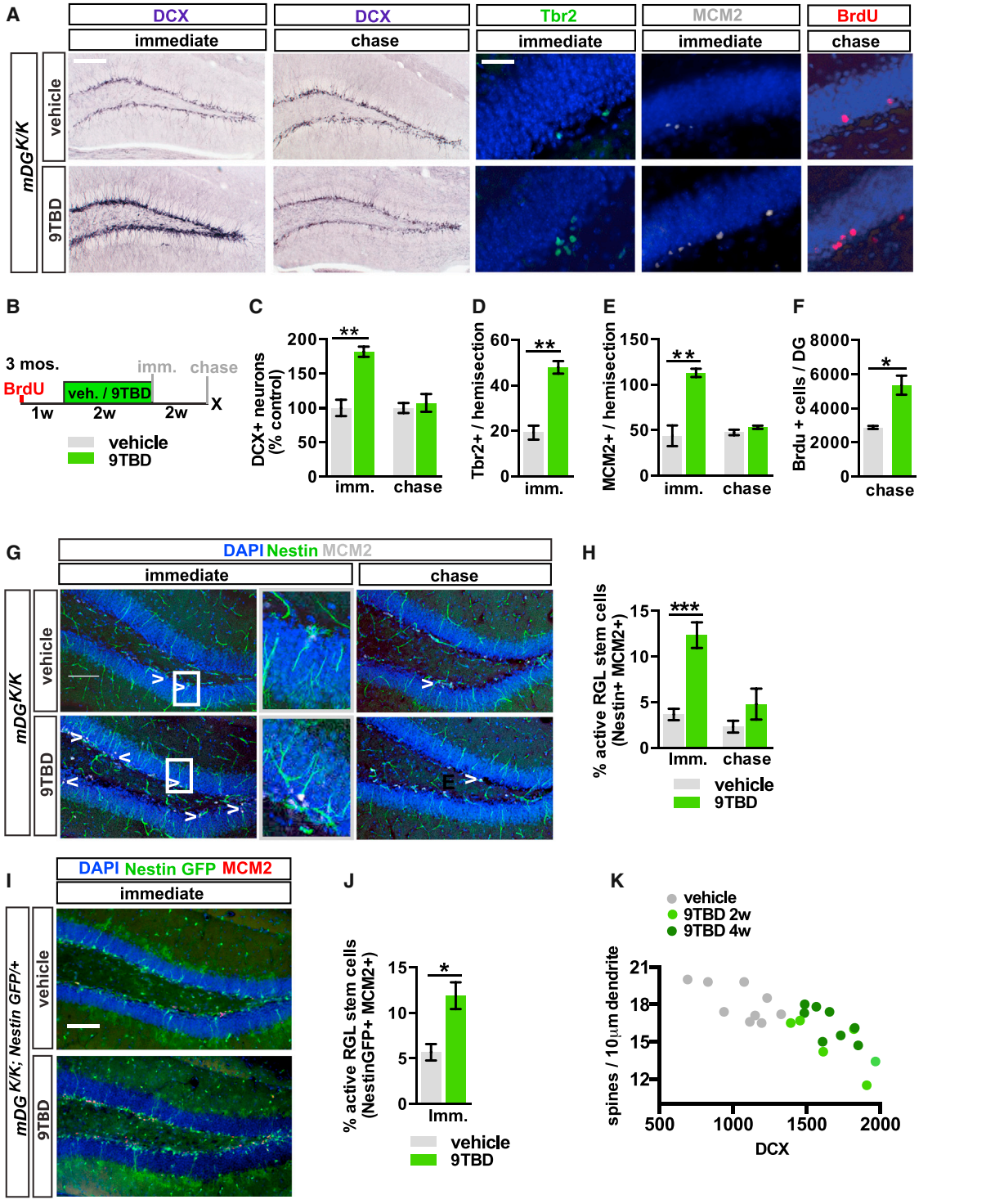

Figure 3. Reversible Overexpression of *Klf9* in Mature DGCs Modulates Activation of NSCs and Neuronal Competition Dynamics

(A–F) Adult hippocampal neurogenesis is reversibly enhanced in $mDG^{K/K}$ mice. (A) Images show labeling for DCX, Tbr2, MCM2, and BrdU. (B) Schematic indicates experimental design for (A) and (C)–(J). (C) Reversible expansion of the DCX+ population in 9TBD-treated $mDG^{K/K}$ mice (n = 5, 3 immediate; n = 6, 7 chase). (D) Increased number of progenitors (Tbr2+), (E) reversible enhancement of dividing cells (MCM2+) (n = 3, 3), and (F) enhanced survival of 5-week-old adult-born cells in GCL of 9TBD-treated $mDG^{K/K}$ mice (n = 3, 3).

(legend continued on next page)

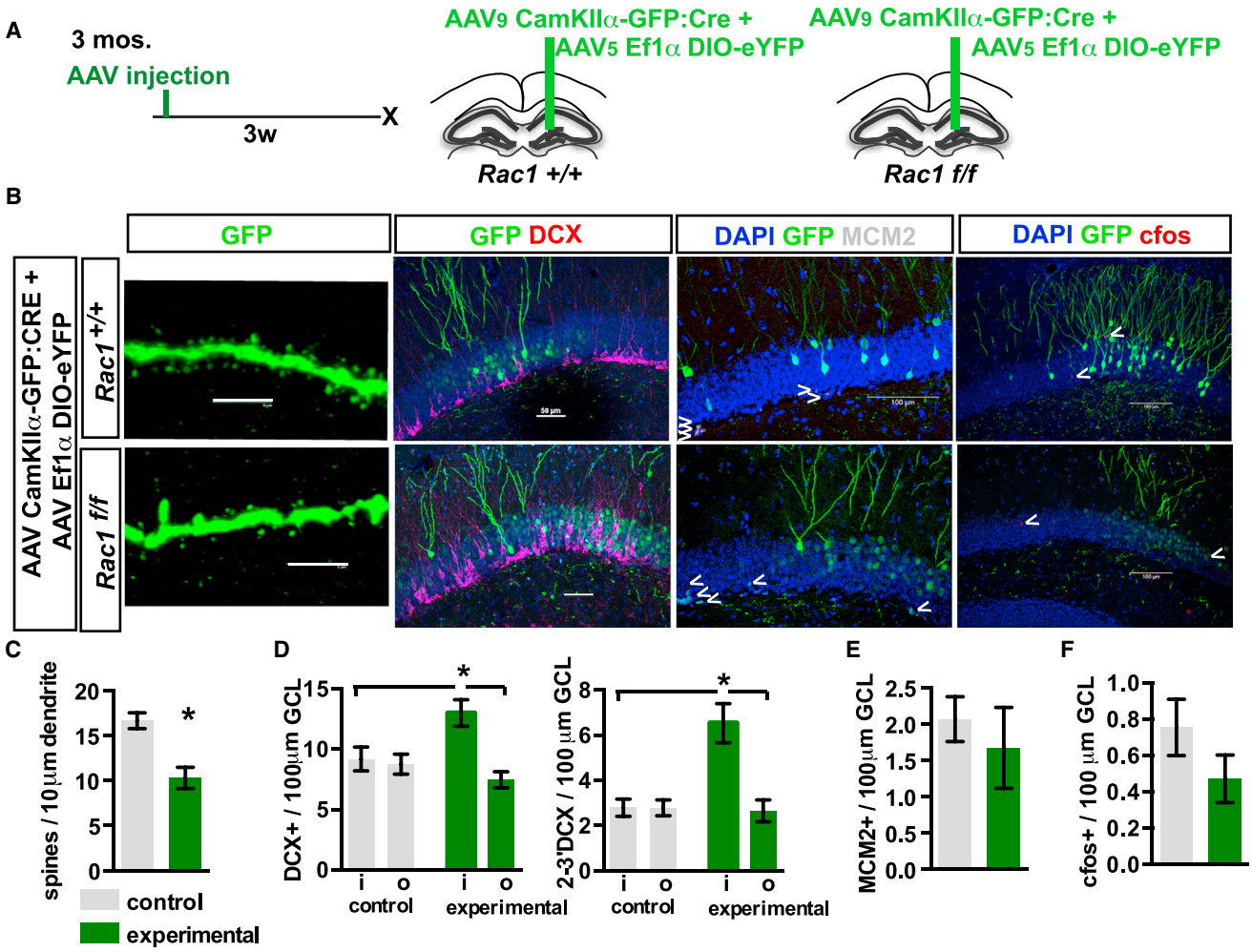

Figure 4. Conditional Elimination of *Rac1* in Mature DGCs Decreases Spine Density and Increases the Survival of Adult-Born DGCs

(A–D) Elimination of Rac1 expands the DCX+ population of adult-born DGCs. (A) Timeline and viral system. (B) Representative images of (left to right): OML dendritic segments, DCX, MCM2, and c-fos from Rac1 WT (top, AAV_9-CaMKIIα-Cre:GFP/AAV_5-EF1α-DIO-eYFP-injected $Rac1^{+/+}$ animals) and Rac1-negative neurons (bottom, $Rac1^{f/f}$ animals) 3 weeks after virus infection (scale bars, left to right, represent 5 μm, 50 μm, 100 μm, and 100 μm). (C) Inducible loss of *Rac1* reduces dendritic spine density (n = 7, 5). Control group also includes AAV_9-CaMKIIα-GFP/AAV_5-EF1α-DIO-eYFP-injected $Rac1^{f/f}$ animals to control for potential genotype effects (n = 4 of 7). (D) Inducible loss of *Rac1* increases the total DCX+ population (left) and the more mature DCX+ population (right) only in the area in which Cre virus is expressed in $Rac1^{f/f}$ animals.

(E and F) Inducible loss of *Rac1* does not affect the MCM2+ population (E) or c-fos expression (F) in the virally transduced neurons (n = 7, 5). Data are represented mean ± SEM.

Conditional Elimination of *Rac1* in Mature DGCs Decreases Spine Density and Increases the Survival of Adult-Born DGCs

To independently determine whether dendritic spine elimination in mature DGCs dictates integration of adult-born DGCs, we designed a strategy to acutely delete the Rho family GTPase Rac1, a cytoskeletal regulator of spines, in a small population of mature DGCs (Tada and Sheng, 2006) (Figure 4A). We injected the upper blade of the dorsal DG in $Rac1^{f/f}$ mice and $Rac1^{+/+}$ littermates with AAV viruses expressing Cre and conditional eYFP or eGFP to infect a small population of mature DGCs (DCX−, data not shown). Three weeks following infection, we found that acute elimination of *Rac1* decreased mature DGC OML spine density (Figures 4B and 4C, t test, control versus Rac1, p = 0.0101) without affecting activity (Figures 4B and 4F). Analysis of the density of DCX+ cells revealed a small but significant

(G–J) NSC activation is reversibly enhanced in $mDG^{K/K}$ mice. (G) Representative images of activation of NSCs (arrowheads, Nestin+ MCM2+) with boxes to indicate magnified region. (H) Quantification of G (n = 7, 7). (I) Representative images of activated NSCs in vehicle- and 9TBD-treated $mDG^{K/K;\ NestinGFP/+}$ mice. (J) Quantification of (I) (n = 3, 4).

(K) Dendritic spine density of mature DGCs is inversely correlated with the number of DCX+ cells in dorsal DG. Dots represent individual animals. Scale bar represents 100 μm and 20 μm in (A) and 100 μm (G) and (I). Data are represented mean ± SEM.

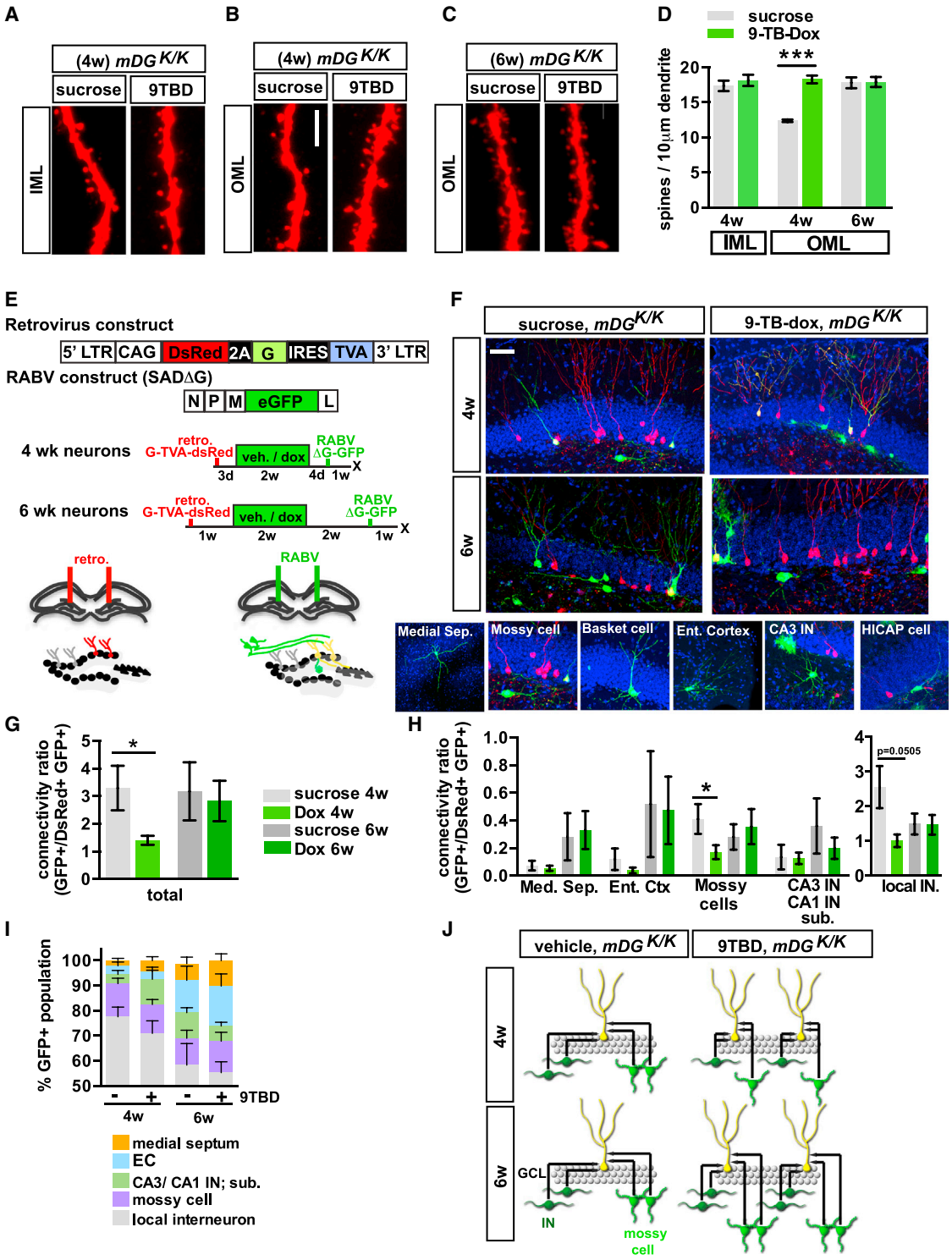

Figure 5. Genetic Enhancement of Adult Hippocampal Neurogenesis Transiently Reorganizes Local Afferent Connectivity of Maturing Adult-Born DGCs

(A–D) 4- but not 6-week-old adult-born DGCs of 9TBD-treated *mDG*$^{K/K}$ mice have greater spine density than vehicle-treated *mDG*$^{K/K}$ mice. Maximum intensity projections of confocal z stack scans of (A and C) OML and (B) IML dendritic segments 4 weeks (A and B) or 6 weeks (C) after injection of DsRed-expressing retrovirus. 9TBD was administered as shown in (E). (D) Quantification of (A)–(C) (4 weeks n = 5, 4; 6 weeks n = 3, 3).

(legend continued on next page)

increase in the DCX+ population within the zone of mature DGCs with reduced dendritic spines (i = "inside" the region of viral expression, o = "outside" corresponding region on the contralateral section; one-way ANOVA, $F = 5.617$, $p = 0.0058$, n = 7,5, con. i versus con. o: ns, con. i versus Rac1 i: $p < 0.05$, Rac1 o versus Rac1 i: $p < 0.05$). Within this sample, there was a larger increase in the DCX+ population with secondary and tertiary dendrites (one-way ANOVA, $F = 12.2$, $p < 0.0001$, n = 7,5, con. i versus con. o: ns, con. i versus Rac1 i: $p < 0.05$, Rac1 o versus Rac1 i: $p < 0.05$; fold increase total DCX 1.42 ± 0.12, fold increase 2-3 DCX 2.33 ± 0.31 t test $p = 0.0241$, Figures 4B and 4D). However, elimination of *Rac1* did not affect the size of the dividing population expressing MCM2 (Figures 4B and 4E). These observations strongly suggest that reduction of mature DGC spine density is sufficient to promote expansion of the integrating DCX+ population.

Genetic Enhancement of Adult Hippocampal Neurogenesis Transiently Reorganizes Local Afferent Connectivity of Maturing Adult-Born DGCs

To understand how the topographic organization of inputs to adult-born DGCs is modified by enhancing their integration, we employed retroviral labeling and pseudo-typed rabies virus *trans*-synaptic tracing (Wickersham et al., 2007; Vivar et al., 2012; Deshpande et al., 2013; Bergami et al., 2015). Infection with modified rabies virus (ENV-A pseudotyped RABV lacking G glycoprotein and expressing GFP, SADΔG-GFP, Figure 5E) (Wickersham et al., 2007) is restricted to a specific, labeled population of starter cells expressing the avian receptor TVA and limits tracing to first-order pre-synaptic partners, as further *trans*-synaptic is abrogated in the absence of G. Here, we injected retroviruses expressing DsRed-2A-G-IRES-TVA into dorsal DG of $mDG^{K/K}$ mice prior to treatment with vehicle or 9TBD, followed by DG injections of RABV (SADΔG-GFP) 3 or 5 weeks following retroviral infection. Mice were sacrificed 1 week post-RABV infection (Figure 5E). We did not see a difference in the general morphology of the 4- and 6-week-old adult-born DGCs from vehicle- and 9-TBD-treated mice (Figures S4F–S4I), nor did we see a difference in size or number of MFT-filopodia of 5-week-old DGCs labeled with retrovirus expressing tdTomato (Figures S4C–S4E). However, 4-week-old, but not 6-week-old, adult-born DGCs of 9TBD-treated $mDG^{K/K}$ mice showed a significant increase in dendritic spine density in the OML (Figures 5A–5D, t test, 4 week vehicle versus 9TBD, $p < 0.0001$). We observed inputs from local (DG hilus, GCL, and ML) interneurons (INs) and mossy cells, CA3 interneurons, and long-range projections from neurons of the medial septum and entorhinal cortex (EC) (Vivar et al., 2012, 2016; Deshpande et al., 2013; Bergami et al., 2015). Using location, morphology, and marker expression (data not shown) the GFP-only positive presynaptic neurons within the DG were identified as glutamatergic hilar mossy cells or distinct types of GABAergic interneurons distributed between the hilus (e.g., HIPP cells), the SGZ/GCL (e.g., basket cells, HICAP cells), and the molecular layer (ML; e.g., MOPP and axo-axonic cells). 4-week-old adult-born DGCs of 9TBD-treated $mDG^{K/K}$ mice had a significantly lower connectivity ratio (t test, vehicle versus 9TBD, $p = 0.0262$) that appears to be driven by decreased connectivity with mossy cells (t test, vehicle versus 9TBD, $p = 0.03$) and DG INs (t test, vehicle versus 9TBD, $p = 0.0505$, Figures 5G and 5H). In contrast, 6-week-old adult-born DGCs in vehicle- and 9TBD-treated $mDG^{K/K}$ mice exhibited similar connectivity ratios (Figures 5G and 5H). We did not see a difference between vehicle- and 9TBD-treated mice in the relative proportions of afferent inputs from each identified region (Figure 5I). Thus, the expanded cohort of adult-born DGCs in $mDG^{K/K}$ mice shows equivalent afferent synaptic connectivity upon maturation.

Genetic Expansion of a Cohort of 5- to 8-Week-Old Adult-Born DGCs Decreases Spatial Interference and Enhances Long-Term Memory Strength and Precision

Loss-of-function and electrophysiological studies support a critical role for 4- to 8-week-old adult-born DGCs in memory processing (Snyder et al., 2001; Schmidt-Hieber et al., 2004; Saxe et al., 2006; Ge et al., 2007; Denny et al., 2012; Gu et al., 2012; Marín-Burgin et al., 2012). To assess the impact of expanding a cohort of 5- to 8-week-old adult-born DGCs on hippocampal-dependent memory functions, we extended the chase period following *Klf9* overexpression to 4 weeks before starting behavioral testing. 9TBD-treated adult mice showed normal innate anxiety, behavioral despair, and modestly improved novel object recognition memory (Figures S5A–S5F). Both vehicle- and 9TBD-treated adult mice located the hidden platform in the Morris water maze with comparable latencies (ANOVA, day: $F_{(8,144)} = 33.52$, $p < 0.0001$, treatment: $F_{(1,18)} = 0.1187$, $p = 0.7344$, interaction: $F_{(8,144)} = 0.6848$, $p = 0.8016$) and swim speed (data not shown) during the acquisition phase (days 1–9) and preferred the target quadrant during the first probe trial on day 10 (Figures 6A–6C) (ANOVA, vehicle: $F = 3.46$, $p = 0.0262$, target versus left, opposite $p < 0.05$; 9TBD: $F = 8.4$, $p = 0.0002$, target versus left, right, opposite $p < 0.05$). We then assessed reversal spatial learning by switching the platform location to the opposite quadrant. Both vehicle- and 9TBD-treated $mDG^{K/K}$ mice showed similar latencies to reach the platform in the new location (ANOVA, day: $F_{(4,72)} = 14.43$, $p < 0.0001$, treatment: $F_{(1,18)} = 1.492$, $p = 0.2376$, interaction: $F_{(4,72)} = 0.8749$, $p = 0.4833$, Figure 6D). However, in a probe trial on day 3 of the reversal phase, only the mice with an expanded cohort of 5- to 8-week-old adult-born neurons preferred the new target location (Figure 6E, ANOVA, vehicle: $F = 0.64$, $p = 0.5942$; 9TBD: $F = 5.97$, $p = 0.0021$,

(E–J) Decreased local monosynaptic inputs onto 4-week-old, but not 6-week-old, adult-born DGCs in 9TBD-treated $mDG^{K/K}$ mice. (E) Schematic showing rabies virus constructs and injection paradigm for (F)–(J). (F) Representative images of dorsal DG sections showing retrovirally labeled cells (red), starter cells (yellow), and presynaptic partners (green). Bottom: images of specific presynaptic cell types. (G) Connectivity ratio of 4-week-old, but not 6-week-old, adult-born DGCs is decreased in 9TBD-treated $mDG^{K/K}$ mice relative to controls (n = 4 for all groups) with (H) specific reductions in connectivity to mossy cells and interneurons (n = 4 DG INs $p = 0.0505$). (I) 4- and 6-week-old adult-born DGCs of vehicle- and 9TBD-treated $mDG^{K/K}$ show similar distributions of pre-synaptic cells. (J) Population-level model conveying how enhancing adult hippocampal neurogenesis reorganizes inputs from mossy cells and DG INs. Scale bar represents 5 μm in (A) and (C) and 20 μm in (F). Data are represented mean ± SEM.

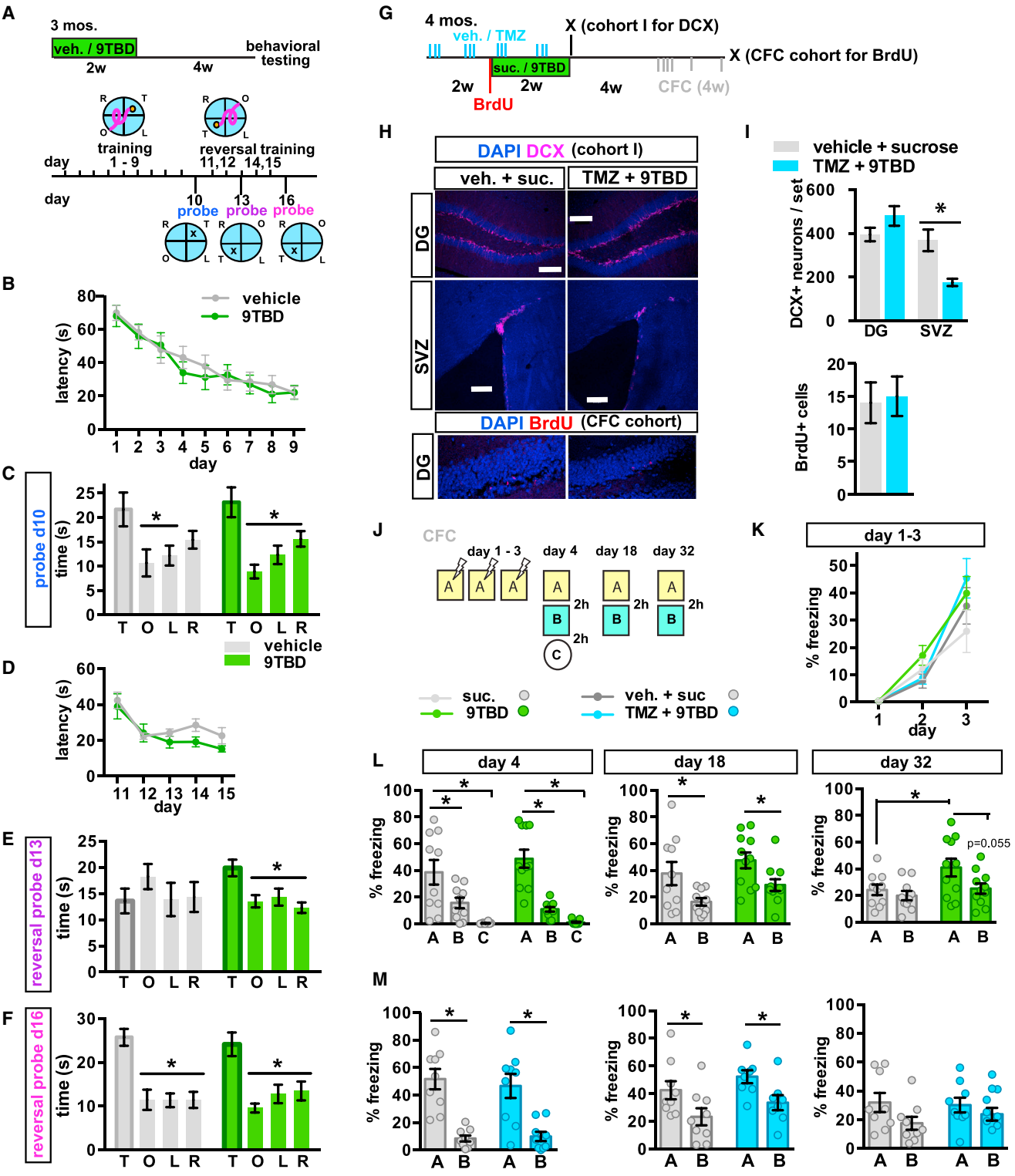

Figure 6. Genetic Expansion of a Cohort of 5- to 8 Week-Old Adult-Born DGCs Decreases Spatial Interference and Enhances Long-Term Memory Strength and Precision

(A–F) (A) Schematic of MWM paradigm used in (B)–(F). (B) Vehicle- and 9TBD-treated *mDG*$^{K/K}$ mice exhibit similar latencies to locate the hidden platform across training days (n = 10, 10). (C) Both groups preferred the target quadrant during the probe trial on day 10. (D) Vehicle- and 9TBD-treated *mDG*$^{K/K}$ mice exhibit similar latencies to locate the hidden platform during training at the reversal location. (E) In the first reversal probe (day 13 prior to training) 9TBD-treated *mDG*$^{K/K}$

(legend continued on next page)

target versus left, right, opposite $p < 0.05$), while the control group perseverated in the original target location, only acquiring the same level of performance with 3 additional days of training (Figure 6F, ANOVA, vehicle: $F = 313.79$, $p < 0.0001$, target versus left, right, opposite $p < 0.05$; 9TBD: $F = 9.166$, $p = 0.0001$, target versus left, right, opposite $p < 0.05$). In a separate series of experiments, we found that mice with reversible overexpression of *Klf9* only in CA1 showed no improvement in cognitive flexibility in the reversal learning task (Figure S5J–S5Q).

Using a behaviorally naive cohort of adult $mDG^{K/K}$ mice, we examined the effect of expanding the cohort of 5- to 8-week-old adult-born DGCs on contextual fear discrimination memory. While both groups of mice showed comparable acquisition of contextual fear learning on days 1–3 (ANOVA, day: $F_{(2,38)} = 34.66$, $p < 0.0001$, treatment: $F_{(1,19)} = 1.997$, $p = 0.2732$, interaction: $F_{(2.38)} = 1.053$, $p = 0.3590$) and contextual fear discrimination on day 4 (ANOVA A versus B, context: $F_{(1,19)} = 42.71$, $p < 0.0001$, treatment: $F_{(1,19)} = 0.1384$, $p = 0.714$, interaction: $F_{(1,19)} = 2.606$, $p = 0.123$; t test, A versus B, vehicle: $p = 0.0352$, 9TBD: $p = 0.0006$, ANOVA A versus C, context: $F_{(1,19)} = 58.99$, $p < 0.0001$, treatment: $F_{(1,19)} = 0.8742$, $p = 0.3615$, interaction: $F_{(1,19)} = 0.7341$, $p = 0.4022$; t test, A versus C, vehicle: $p < 0.0001$, 9TBD: $p < 0.0001$) and 2 weeks post-training (ANOVA, context: $F_{(1,19)} = 18.18$, $p = 0.004$, treatment: $F_{(1,19)} = 2.494$, $p = 0.1308$, interaction: $F_{(1,19)} = 0.0061$, $p = 0.9384$; t test, A versus B, vehicle: $p = 0.0333$, 9TBD: $p = 0.0209$), the mice with more 5- to 8-week-old adult-born DGCs exhibited modestly stronger contextual fear memory and context discrimination 4 weeks post-training (ANOVA, context: $F_{(1,19)} = 1.834$, $p = 0.0213$, treatment: $F_{(1,19)} = 4.152$, $p = 0.0558$, interaction: $F_{(1,19)} = 2.048$, $p = 0.1686$; t test, A versus B, 9TBD: $p = 0.0546$; vehicle A versus 9TBD A: $p = 0.0495$, Figures 6J–6L).

To determine whether these cognitive improvements were due to increased adult hippocampal neurogenesis and not to other processes, such as reversible spine elimination, we utilized a pharmacological strategy (Garthe et al., 2009; Akers et al., 2014) to occlude the enhancement in neurogenesis in 9TBD-treated $mDG^{K/K}$ mice. Administration of saline (vehicle) or temozolomide (TMZ, i.p. 3×/week), a DNA alkylating agent that causes cell death of dividing cells, to adult $mDG^{K/K}$ mice prior to and during sucrose or 9TBD treatment (Figure 6G) blocked enhancement of DG neurogenesis and significantly reduced SVZ neurogenesis (t test, n = 4,5, vehicle/sucrose versus TMZ/9TBD DG $p = 0.1862$, SVZ $p = 0.0105$) (Figures 6H and 6I). Utilizing this treatment, followed by a 4-week chase, period both vehicle/sucrose- and TMZ/9TBD-treated groups showed comparable acquisition of contextual fear learning (ANOVA, day: $F_{(2,32)} = 61.26$, $p < 0.0001$, treatment: $F_{(1,16)} = 0.8728$, $p = 0.3641$, interaction: $F_{(2,32)} = 1.025$, $p = 0.3703$, Figure 6K) and comparable contextual fear discrimination on day 4 (ANOVA, context: $F_{(1,16)} = 45.86$, $p < 0.0001$, treatment: $F_{(1,16)} = 0.0737$, $p = 0.7895$, interaction: $F_{(1,16)} = 0.2951$, $p = 0.5945$; t test, A versus B, vehicle/sucrose: $p < 0.0001$, TMZ/9TBD: $p = 0.0013$), and at 2 weeks post-training (ANOVA, context: $F_{(1,16)} = 49.11$, $p < 0.0001$, treatment: $F_{(1,16)} = 1.629$, $p = 0.2213$, interaction: $F_{(1,16)} = 0.0075$, $p = 0.9319$; t test, A versus B, vehicle: $p = 0.0482$, 9TBD: $p = 0.0198$). Neither group showed discrimination at 4 weeks post-training (Figure 6M).

Contextual Memory Precision Is Improved in Middle-Aged and Aged Mice with Expanded Populations of 5- to 8-Week-Old Adult-Born DGCs

Analysis of *Klf9* transcripts in 9TBD-treated 11- and 17-month-old $mDG^{K/K}$ mice showed a robust elevation in *Klf9* levels in the DG but not CA3 or CA1 (Figures S6A and S6B, 17 months data not shown). Immediately following 2 weeks of 9TBD treatment, middle-aged and aged $mDG^{K/K}$ mice showed a significant expansion in the DCX+ population (vehicle versus 9TBD t test, 11 months $p = 0.0137$, 5.9- ± 1.11-fold increase; 17 months, vehicle versus 9TBD $p = 0.0004$, 7.63- ± 0.88-fold increase) and ~2-fold increase in survival in 3-week-old cells (Figures 7A, 7B, 7D, and 7E, t test, 11 months, vehicle versus 9TBD $p = 0.0004$; t test, 17 months, vehicle versus 9TBD $p = 0.0441$). Additionally, in middle-aged and aged mice, *Klf9* overexpression in mature DGCs robustly activated NSCs (Figures 7A and 7C, t test vehicle versus 9TBD, middle-aged $p = 0.0277$; aged $p < 0.0001$) and in middle aged mice increased the number of Tbr2+ (5.5- ± 0.24-fold increase) and MCM2+ cells (3.6 ± 0.22-fold increase, Figures S6C–S6E). Importantly, these observations suggest that we can rejuvenate the DG of middle-aged and aged mice with adult-born DGCs to match the size of the adult-born DGC population in ~5- to 6-month-old mice (Figure 7B).

We next sought to examine the effects of expanding a cohort of 5- to 8-week-old adult-born DGCs in middle-aged and aged mice on contextual fear discrimination (Figures 7F–7H). 12-month-old 9TBD- and vehicle-treated $mDG^{K/K}$ mice showed comparable acquisition of contextual fear learning (ANOVA, day: $F_{(1,16)} = 0.0028$, $p < 0.0001$, treatment: $F_{(1,16)} = 50.54$,

mice, but not controls, spent significantly more time in the target quadrant, whereas (F) both groups spent similar amounts of time swimming in the target quadrant during the probe trial on day 16.

(G–I) Concurrent TMZ treatment prevents *Klf9*-overexpression-induced expansion of the adult-born neuron population. (G) Schematic of TMZ and 9TBD dosing used for (H), (I), (K), and (M). (H) Representative images show no change in the DCX+ population of adult-born DGCs but a reduction in DCX+ adult-born neurons in the SVZ in TMZ/9TBD-treated $mDG^{K/K}$ mice. Scale bars represent 200 μm. Bottom: representative images of BrdU labeling as described in (I). (I) Top: in the DG, TMZ treatment prevents *Klf9*-overexpression-induced increase in neurogenesis (n = 4), and in the SVZ, where *Klf9* overexpression does not affect neurogenesis, TMZ treatment significantly reduced neurogenesis (n = 4, 5). Bottom: quantification of DG BrdU+ cells shows no change. BrdU was given at the start of 9TBD or sucrose treatment (i.e., halfway through the vehicle or TMZ treatment paradigm) and animals were sacrificed after CFC testing was completed (n = 4, 4).

(J–M) Expansion of the 5- to 8-week-old adult-born DGC population improves memory precision. (J) Schematic of the contextual fear conditioning paradigm. (K) Vehicle- and 9TBD-treated (n = 10, 11), and vehicle/sucrose- and TMZ/9TBD-treated (n = 8, 8) $mDG^{K/K}$ mice exhibited comparable acquisition of contextual fear memory over 3 days. (L) 9TBD-treated $mDG^{K/K}$ mice exhibited modestly improved discrimination of similar contexts at day 32 (t test, A versus B, 9TBD: $p = 0.0546$) and enhanced long-term contextual fear memory at day 32 (t test, vehicle A versus 9TBD A: $p = 0.0495$). (M) Vehicle/sucrose- and TMZ/9TBD-treated $mDG^{K/K}$ mice showed no differences in discrimination at day 4, 18, or 32. For CFC data, graphs show mean ± SEM with individual animals shown as circles.

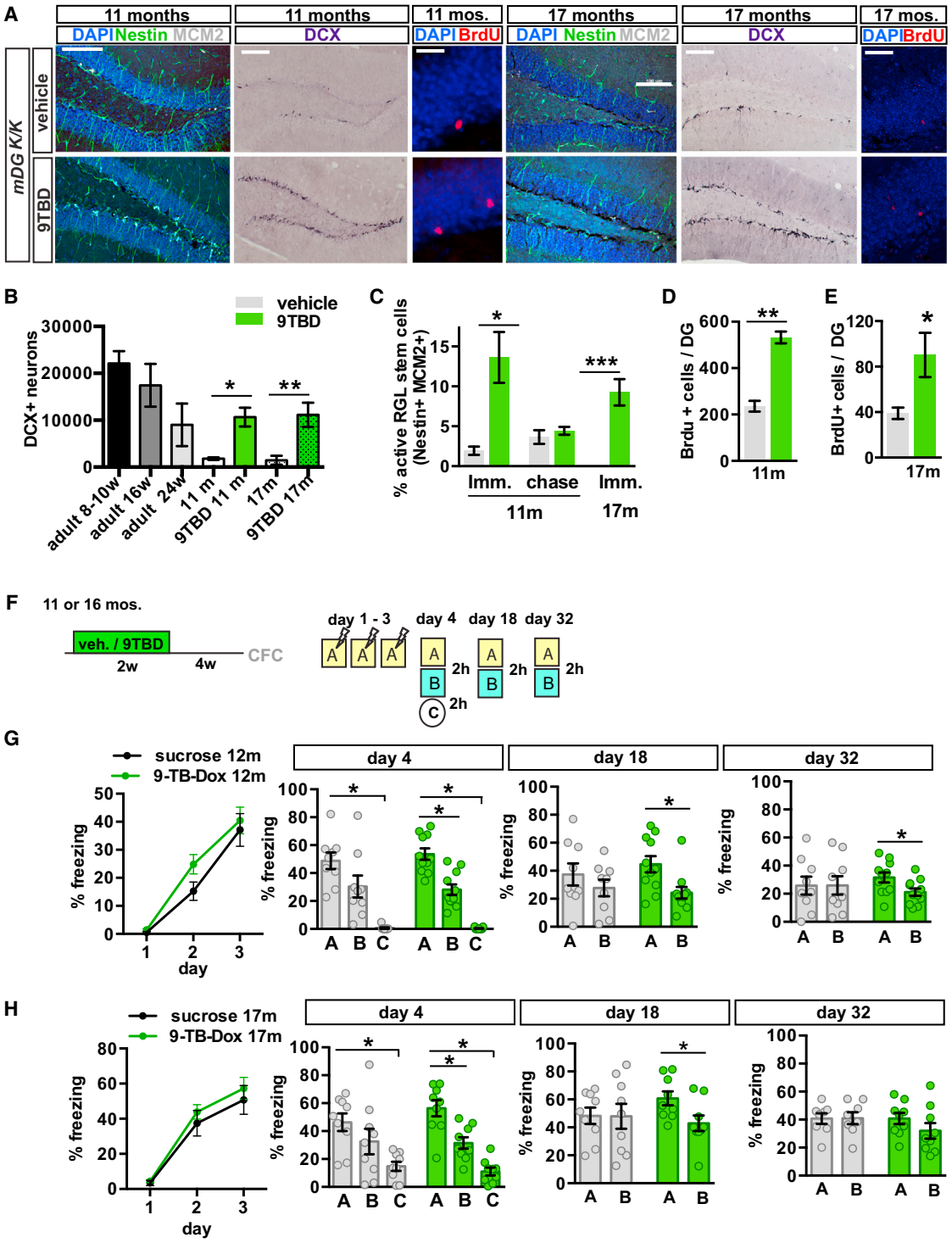

Figure 7. Contextual Memory Precision Is Improved in Middle-Aged and Aged Mice with Expanded Populations of 5- to 8-Week-Old Adult-Born DGCs

(A–E) Enhancement of adult hippocampal neurogenesis in middle-aged and aged *mDG*$^{K/K}$ mice. (A) Representative hippocampal images from 11- and 17-month-old vehicle- or 9TBD-treated *mDG*$^{K/K}$ mice showing labeling for DCX, Nestin, and MCM2 (activated NSCs), and BrdU. (B) The DCX+ population is increased in 9TBD-treated *mDG*$^{K/K}$ mice at 11 months (10,667 ± 2,011) and 17 months old (11,160 ± 1,286) to levels comparable to that of 5- to 6-month-old

(legend continued on next page)

p = 0.3050, interaction: $F_{(1,16)}$ = 0.9218, p = 0.4969), but the 9TBD group, unlike the controls, discriminated between the similar contexts A and B at days 4 (ANOVA, context: $F_{(1,16)}$ = 50.54, p < 0.0001, treatment: $F_{(1,16)}$ = 0.0029, p = 0.958, interaction: $F_{(1,16)}$ = 0.9218, p = 0.3513; t test, A versus B, 9TBD: p = 0.0002), 18 (ANOVA, context: $F_{(1,16)}$ = 15.44, p = 0.001, treatment: $F_{(1,16)}$ = 0.0687, p = 0.7963, interaction: $F_{(1,16)}$ = 1.980, p = 0.1764; t test, A versus B, 9TBD: p = 0.0096), and 32 (ANOVA, context: $F_{(1,16)}$ = 2.404, p = 0.1384, treatment: $F_{(1,16)}$ = 0.0072, p = 0.9333, interaction: $F_{(1,16)}$ = 2.526, p = 0.1294; t test, A versus B, 9TBD: p = 0.0274). In contrast, both groups discriminated between the training context A and the distinct context C at day 4 (Figure 7G) (ANOVA, context: $F_{(1,16)}$ = 202.4, p < 0.0001, treatment: $F_{(1,16)}$ = 0.1976, p = 0.6626, interaction: $F_{(1,16)}$ = 0.2720, p = 0.6091; t test, A versus C, vehicle, 9TBD: p < 0.0001). *mDG*$^{K/K}$ mice with an expanded cohort of 5- to 8-week old adult-born DGCs that had been behaviorally tested in the CFC paradigm were aged to 16 months and *Klf9* overexpression in mature DGCs was re-induced to expand another population of adult-born DGCs. Prior to re-induction, all the mice were found to not have any detectable memory (freezing behavior) of the shock context (data not shown). 9TBD- and vehicle-treated 17-month-old *mDG*$^{K/K}$ mice showed normal innate anxiety behavior as assessed in the open field and light-dark paradigms (Figures S5G–S5I). Both groups of aged *mDG*$^{K/K}$ mice showed comparable acquisition of contextual fear learning (ANOVA, day: $F_{(2,32)}$ = 77.54, p < 0.0001, treatment: $F_{(1,16)}$ = 0.5951, p = 0.4517, interaction: $F_{(2,32)}$ = 0.2964, p = 0.7455), and both groups discriminated between the training context A and the distinct context C at day 4 (Figure 7H, ANOVA, context: $F_{(1,16)}$ = 124.6, p < 0.0001, treatment: $F_{(1,16)}$ = 0.2888, p = 0.5984, interaction: $F_{(1,16)}$ = 4.035, p = 0.0617; t test, A versus C, vehicle: p = 0.0004, 9TBD: p < 0.0001). However, the 9TBD group, unlike the controls, discriminated between the similar contexts A and B at days 4 (ANOVA, context: $F_{(1,16)}$ = 17.57, p = 0.0007, treatment: $F_{(1,16)}$ = 0.3038, p = 0.5891, interaction: $F_{(1,16)}$ = 1.463, p = 0.244; t test, A versus B, 9TBD: p = 0.0029) and 18 (ANOVA, context: $F_{(1,16)}$ = 32.62, p = 0.0898, treatment: $F_{(1,16)}$ = 0.2397, p = 0.6311, interaction: $F_{(1,16)}$ = 3.022, p = 0.1013; t test, A versus B, 9TBD: p = 0.0292). Neither group discriminated between the similar contexts A and B at day 32. Together, these observations suggest that expanding the population of 5- to 8-week-old adult-born DGCs in middle-aged and aged mice improves contextual memory precision.

Expansion of a Cohort of 5- to 8-Week-Old Adult-Born DGCs Enhances Global Remapping in the DG

Because mice with expanded populations of 5- to 8-week-old adult-born DGCs exhibited improved behavioral discrimination under conditions of high, but not low, interference (similar but not distinct contexts), we asked whether enhancing adult hippocampal neurogenesis affects global remapping in the DG. We utilized catFISH (cellular compartment analysis of temporal activity using fluorescence in situ hybridization) to visualize cellular assemblies activated in the DG by two temporally separated exposures to contexts based on nuclear and cytoplasmic localization of c-*fos* transcripts (Guzowski and Worley, 2001). Adult 9TBD- and vehicle-treated *mDG*$^{K/K}$ mice, and an additional cohort of *mDG*$^{K/K}$ mice treated with vehicle/sucrose and TMZ/9TBD (as in Figure 6G), were conditioned to a foot shock in context A over 3 days followed by one of three different context exposure conditions on day 4 (A-A, A-B, or A-C, Figures 8C–8E and 8G). Analysis of activated cell assemblies in the DG of controls in the A-A condition showed significantly higher levels of reactivation (cells positive for both nuclear and cytoplasmic transcripts, i.e., percentage of overlap) than control mice of A-C group (t test, vehicle A-A versus vehicle A-C, p = 0.0391) but similar overlap as control mice in the A-B group (Figures 8C–8D and 8G; Figure S7). Further, the ventral DG showed significantly greater overlap than dorsal DG in control mice (Figures 8C–8E and 8G; Figure S7; t test, vehicle dorsal versus ventral, A-A: p = 0.0009, A-B: p < 0.0001, A-C: p = 0.0585). In contrast to control animals, analysis of 9TBD-treated *mDG*$^{K/K}$ mice revealed significantly less reactivation in mice exposed to A-B than A-A (t test, 9TBD A-A versus A-B p = 0.0296). Importantly, in the high-interference A-B condition, mice with expansion of the adult-born DGC population showed significantly less re-activation of DG cellular assemblies (t test, vehicle versus 9TBD, dorsal p = 0.0063, ventral p = 0.0061) than vehicle-treated *mDG*$^{K/K}$ mice (Figure 8D; Figure S7). Notably, this decrease in reactivation was dependent on the expanded cohort of 5- to 8-week-old adult-born neurons, as no difference in re-activation of cellular assemblies was seen between vehicle/sucrose- and TMZ/9TBD-treated *mDG*$^{K/K}$ mice (Figure 8E; Figure S7). Middle-aged 9TBD-treated *mDG*$^{K/K}$ mice exposed to A-B also showed significantly less re-activation of DG cellular assemblies than vehicle-treated *mDG*$^{K/K}$ mice (t test, vehicle versus 9TBD, dorsal p = 0.0393; ventral p = 0.0477, Figure 8F; Figure S7). By contrast, 9TBD- and vehicle-treated *mDG*$^{K/K}$ mice exhibited similar levels of re-activation of cellular assemblies in the low interference A-C condition.

Analysis of the total populations activated by each exposure in dorsal DG of adult mice suggested that expanding the population of 5- to 8-week-old adult-born DGCs increased the number of cells activated by the first exposure only in A-B and A-C conditions. Furthermore, mice with more 5- to 8-week-old adult-born DGCs exhibited a significant reduction in the number of cells activated only by the second exposure (Figures 8C–8D and 8G). This increase in mismatch-dependent sparseness

mice (9,000 ± 2,266) (11 months: n = 3, 4; 17 months: n = 4, 4) (C–E). Enhanced (C) activation of NSCs and (D and E) survival of 3-week-old adult-born cells in 9TBD-treated 11- and 17-month-old *mDG*$^{K/K}$ mice (11 months: n = 3, 4; 17 months: n = 3, 3 for survival n = 4, 4).

(F–H) 12- and 17-month-old mice with expanded populations of adult-born neurons show modest enhancements in a contextual fear conditioning task. (F) Schematic of the CFC paradigm used in (G) and (H) (12 months: n = 8, 10; 17 months: n = 9, 9). (G) 12-month-old *mDG*$^{K/K}$ mice with an expanded population of 5- to 8-week-old adult-born DGCs exhibit discrimination of similar contexts at day 4, day 18, and day 32. (H) 17-month-old *mDG*$^{K/K}$ mice with expanded population of 5- to 8-week-old adult-born DGCs exhibit discrimination of similar contexts at day 4 and day 18 but not day 32. Scale bar represents 20 μm (BrdU) and 100 μm (remainder) in (A). Data are represented mean ± SEM.

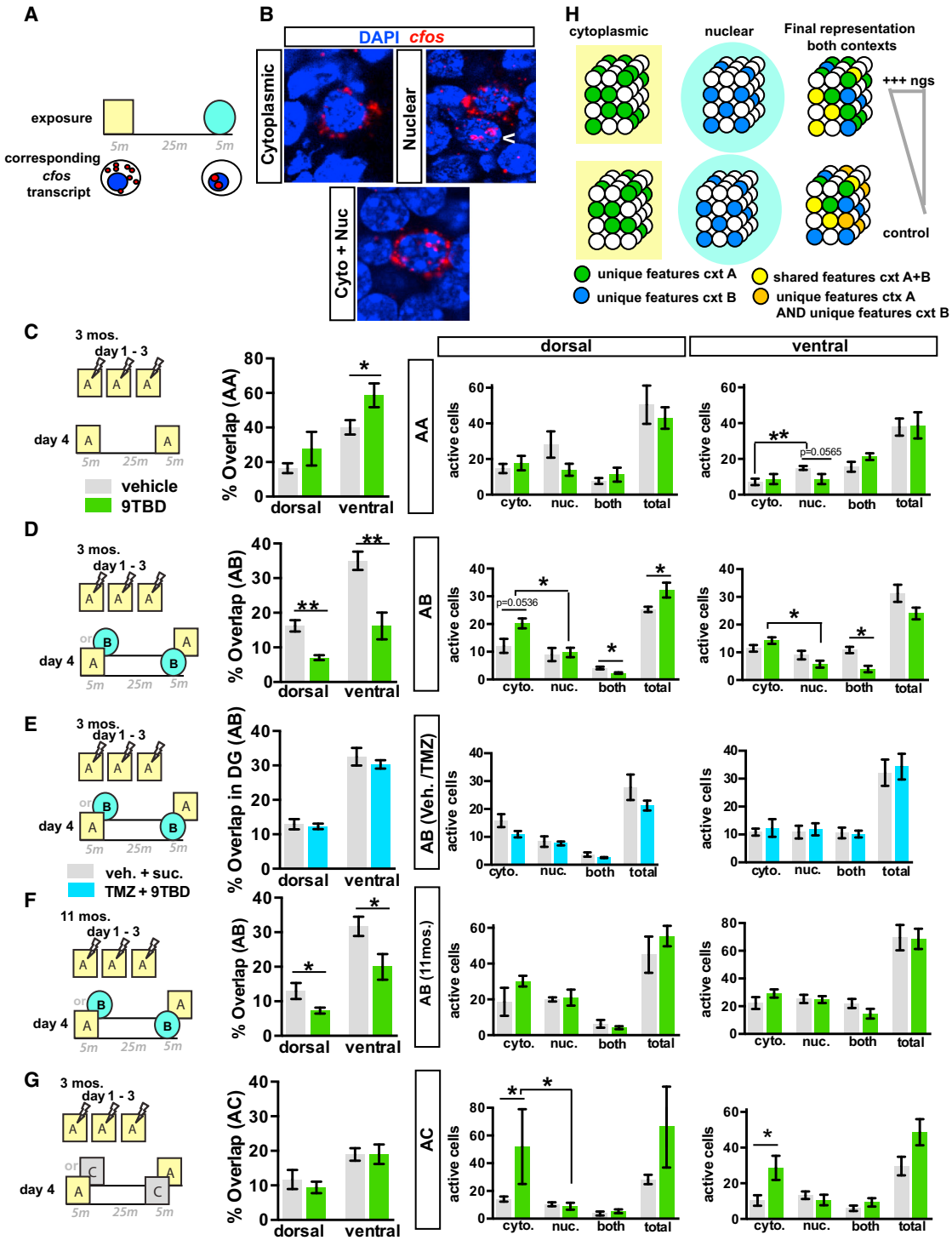

Figure 8. Expansion of a Cohort of 5- to 8-Week-Old Adult-Born DGCs Enhances Global Remapping in the DG

(A) Schematic outlining catFISH concept using c-*fos* intronic and full-length cDNA probes as utilized in (B)–(G).

(B) DGCs exhibiting cytoplasmic, nuclear, or nuclear and cytoplasmic localization of c-*fos* transcripts.

(C) Expanding the cohort of 5- to 8-week-old adult-born DGCs enhances reactivation of DG cellular assemblies in ventral DG following repeat exposure to the same context (ventral A-A, n = 6, 4). Both groups of mice showed similar numbers of active cells (right).

(legend continued on next page)

was lost when the enhancement in neurogenesis was blocked by TMZ (Figure 8E).

DISCUSSION

Mature DGCs are well positioned to link experience and activity with the integration of adult-born DGCs because they receive the vast majority of inputs. Here, we leveraged our identification of Klf9 as a negative regulator of dendritic spines to demonstrate that reversible elimination of OML dendritic spines of mature DGCs enhances the integration of 2- to 3-week-old adult-born DGCs. Inducible loss of Rac1 in mature DGCs also increased this population of adult-born DGCs but did not promote activation of NSCs and progenitors as seen with Klf9 overexpression in mature DGCs. Because reversible Klf9-dependent spine elimination also transiently decreased activity of mature DGCs, we speculate that decreased DGC activity might differentially engage mossy cells and hilar interneurons (Jinde et al., 2012; Song et al., 2012) or alter release of activity-dependent secreted factors (Lie et al., 2005; Ma et al., 2009) to influence NSC and progenitor activation. Alternatively, Klf9's direct transcriptional targets may include pro-neurogenic secreted factors. Our data support the hypothesis that DG neurogenesis is controlled through overlapping, yet discrete, circuit mechanisms, with mature DGC spine density primarily affecting survival of integrating adult-born DGCs and changes in activity or secretome leading to the activation of NSCs and progenitors.

Using RABV tracing in our genetic system, we found that enhancing adult hippocampal neurogenesis did not affect entorhinal cortical connectivity with 4-week-old adult-born DGCs, even though these DGCs had more spines in the OML. However, these DGCs had decreased connectivity with mossy cells and DG-INs (Figure 5J) but unaltered spine density in the IML. These findings raise the possibility that increasing neurogenesis may drive branching of pre-synaptic terminals. In addition, it is thought that mossy cells' glutamatergic and di-synaptic inhibitory inputs coordinate unsilencing of perforant path-excitatory synapses in adult-born DGCs (Vivar et al., 2016; Chancey et al., 2014). Thus, enhancing neurogenesis may induce a transient compensatory rewiring of local connectivity to constrain unsilencing of these perforant path-DGC synapses. As 6-week-old adult-born DGCs were connected to similar numbers of mossy cells and DG-INs, it appears that presynaptic connectivity ratios are scaled up during the maturation of the expanded population of DGCs to restore organization of afferent inputs. It is also possible that 4- to 17-day-old and 7- to 21-day-old adult-born DGCs differ in their ability to compete with mature DGCs, thereby affecting connectivity ratios.

In aging as in adult mice, transient *Klf9* overexpression in mature DGCs robustly enhanced survival of adult-born DGCs, whereas the relative impact on NSC activation is much greater in the aged brain, demonstrating that *Klf9* overexpression in mature DGCs overrides the inhibitory effects of NSC-cell-autonomous, niche-derived, and systemic factors on NSC activation (Hattiangady and Shetty, 2008; Villeda et al., 2011; Encinas and Sierra, 2012). In contrast to adult mice, fear-conditioned middle-aged and aged control mice failed to discriminate the similar context. Expanding the population of 5- to 8-week-old adult-born DGCs in 12- and 17-month-old mice permitted modest discrimination of similar contexts, suggesting a role for adult-born DGCs in resolution of spatial interference that continues during aging.

Expansion of the 5- to 8-week-old adult-born DGC population decreased the overlap between DG ensembles activated by similar contexts in adult and middle-aged mice, an effect that was reversed by pharmacological occlusion of the enhancement in neurogenesis. Interestingly, the degree of overlap in the ventral DG was greater than that of the dorsal DG, thus arguing for differences in efficiency of population-based coding along the DG's septo-temporal axis. A previous study that used *zif268* localization for catFISH analysis in middle-aged rats following a task that required resolution of non-spatial information found uniform levels of global remapping along the septo-temporal axis of the DG (Satvat et al., 2011). Thus, spatial interference may be differentially processed by the dorsal and the ventral DG, much like what has been suggested for CA1 and CA3 based on differences in place cell properties (Jung et al., 1994; Kjelstrup et al., 2008). Simultaneous assessment of population activity in the entorhinal cortex and DG was not measured in these experiments, precluding direct assessment of either input similarity or transformation into divergent outputs, which are emblematic of pattern separation (Neunuebel and Knierim, 2014). However, because the enhancements in global remapping are seen only under conditions of high contextual overlap and require expansion of the adult-born DGC pool, it is likely that these enhancements originate in the DG and are not transferred to the DG from upstream regions.

In mice with expansion of the adult-born DGC population, this decrease in overlap is driven by increased activation of the DG in the first epoch, followed by a suppression of activation in the second epoch in A-B and A-C conditions, but not in the A-A condition. These observations suggest the existence of a neurogenesis-dependent mismatch-detection mechanism that modulates activity of the DG to decrease the overlap of activated ensembles between two consecutive exposures (Burghardt et al., 2012). Interestingly, a previous study found that decreasing adult hippocampal neurogenesis impaired global remapping in CA3 and

(D–F) Expansion of a cohort of 5- to 8-week-old adult-born DGCs (E, n = 6, 6), significantly decreases reactivation of cellular assemblies in dorsal and ventral DG following exposure to similar contexts (A and B) in adult (D) (n = 7, 4) and middle-aged (F) (n = 4, 5) mice. In adult mice, this expansion increases active cells following first exposure and increases sparseness following second exposure (D, right).

(G) Genetic expansion of a cohort of 5- to 8-week-old adult-born DGCs does not affect global remapping in DG in response to a distinct context (n = 6, 3), although the population of active cells following the first exposure is increased (right). Data are represented mean ± SEM.

(H) Model: increasing neurogenesis increases the pool of adult-born DGCs re-activated by features common to both contexts (yellow circles). This in turn decreases the likelihood of re-activating DGCs used to encode unique features of previously experienced contexts (orange circles), thereby decreasing overlap between engrams of contexts A and B.

expanded the active ensemble of CA3 neurons in the second epoch (Niibori et al., 2012). It has been suggested that mature adult-born DGCs respond preferentially to inputs to which they were previously exposed to during their maturation (Tashiro et al., 2007; Aimone et al., 2011; Kropff et al., 2015). Furthermore, adult-born DGCs recruit feedback inhibition to modulate the activity of the DG (Sahay et al., 2011b; Ikrar et al., 2013; Restivo et al., 2015; Temprana et al., 2015). Integrating these observations, we propose a model where adult-born DGCs respond to shared features across similar contexts to suppress activity of the DG and decrease the likelihood of re-activation of mature DGCs that have encode unique features of previously experienced contexts. (Figure 8H) (McAvoy et al., 2015a).

Our findings support a role for inputs onto mature DGCs in modulating adult hippocampal neurogenesis. We demonstrate that neuronal competition dynamics may be harnessed to expand the population of adult-born DGCs across the lifespan to improve memory and population-based coding mechanisms in the DG that support pattern separation. Enhancing adult hippocampal neurogenesis may have therapeutic significance in moderating impairments in pattern separation associated with aging and mild cognitive impairment (Yassa et al., 2010, 2011; Small et al., 2011; Bakker et al., 2012).

EXPERIMENTAL PROCEDURES

Mouse Lines and Animal Care

Generation of TRE-Klf9 mouse line is described in Supplemental Experimental Procedures. The original *CaMKIIα rtTA* line was generated as described (Zhu et al., 2007) with one of the sub-lines described in detail here. All mouse lines were housed four to five per cage in a 12 hr (7:00 a.m. to 7:00 p.m.) light/dark colony room at 22°C–24°C with ad libitum access to food and water. All animals were handled and experiments were conducted in accordance with procedures approved by the Institutional Animal Care and Use Committee at the Massachusetts General Hospital in accordance with NIH guidelines.

9-tert-butyl-doxycycline Administration

Mice were given 2 mg/mL 9-tert-butyl-doxycycline (9TBD) (Echelon Biosciences) in 3% sucrose, or 3% sucrose alone (vehicle), for 14 days in dark bottles. Solutions were freshly prepared and replaced every 3 days. Liquid consumption was monitored for the entire dosing period.

BrdU Injections and Temozolomide Treatment

To assess the survival of adult-born cells in the DG, we administered BrdU via intraperitoneal injection, in 0.9% NaCl at 100, 150, or 200 mg/kg body weight. For injections assessing survival at multiple time points, CldU and IdU were injected and detected as described previously (Stone et al., 2011). Timing of each BrdU injection is described in the accompanying schematic. Mice were given 25 mg/kg temozolomide (TMZ) as described previously (Garthe et al., 2009; Akers et al., 2014). For the final 2 weeks of vehicle or TMZ treatment, the mice were given drinking water with sucrose (vehicle group) or 9TBD (TMZ group) as described above.

In Situ Hybridization and catFISH

Klf-9 riboprobe was generated from the 3′ UTR of mouse *Klf-9* (NM 010638) corresponding to nucleotides 1,500–1,780 as previously described (Scobie et al., 2009). For catFISH experiments, animals experienced two 5 min behavioral episodes 25 min apart and brains were isolated and flash frozen in isopentane on dry ice immediately after the second episode. An intronic c-*fos* probe containing the entire first intron of the *fos* gene (Lin et al., 2011) (generous gift of Dr. Dayu Lin) and a full-length c-*fos* cRNA probe were used to detect nuclear and cytoplasmic c-*fos* transcripts, respectively. Nuclear c-*fos* was defined as puncta colocalizing with DAPI labeling, whereas cytoplasmic labeling was defined as c-*fos*-positive dots surrounding the nucleus.

Immunohistochemistry

Mice were anesthetized with ketamine or xylazine (100 and 2.6 mg/kg body weight, respectively) and transcardially perfused with cold saline, followed by 4% cold paraformaldehyde in PBS. Brains were postfixed overnight in 4% paraformaldehyde at 4°C, then cryoprotected in 30% sucrose and stored at 4°C before freezing in OCT on dry ice. Coronal serial sections (35 μm) were obtained using a Leica cryostat in six matched sets. Immunohistochemistry was performed on one set of tissue as described in the Supplemental Experimental Procedures. Dendritic spine and mossy fiber terminal analysis was performed as described previously (McAvoy et al., 2015b).

Retroviral/Rabies Virus/AAV Injections

Retroviral labeling of adult-born DGCs (Ikrar et al., 2013) and rabies virus *trans*-synaptic tracing was performed as described previously (Deshpande et al., 2013; Bergami et al., 2015). To assess the impact of Rac1 loss, we injected adult male Rac1 floxed (*Rac1*$^{f/f}$) or wild-type (*Rac1*$^{+/+}$) littermates in dorsal DG with AAV_9-CaMKinaseIIα-Cre:GFP and AAV_5-EF1α–DIO-eYFP viruses and mice were sacrificed after 3 weeks.

Contextual Fear Conditioning and Morris Water Maze Tasks

Behavioral assessments were performed as previously described (Sahay et al., 2011a) and are detailed in Supplemental Experimental Procedures.

Statistical Analysis

Statistical tests were carried out as indicated in Supplemental Experimental Procedures.

SUPPLEMENTAL INFORMATION

Supplemental Information includes Supplemental Experimental Procedures and seven figures and can be found with this article online at http://dx.doi.org/10.1016/j.neuron.2016.08.009.

AUTHOR CONTRIBUTIONS

K.M.M., C.R., N.G., P.D., H.V.-R., and S.M.-L. performed experiments. K.N.S., S.B., R.H., M.B., B.B., M.N., M.W., and D.B. contributed reagents and shared resources. A.S. and K.M.M. co-developed the concept, analyzed data, and wrote the manuscript. A.S. conceived the project and supervised all aspects of the project.

ACKNOWLEDGMENTS

We wish to thank members of the A.S. lab and co-authors for their comments on the manuscript, Dr. Dayu Lin for the c-*fos* plasmid, Dr. Karl-Klaus Conzelmann for the rabies virus and Sreyan Chowdhury, Duong Chu and Tomer Langberg for technical assistance. Reagent generation in B.B. lab was supported by German Research Foundation (CRC 1193/1 A02). A.S. is supported by U.S. National Institutes of Health Biobehavioral Research Awards for Innovative New Scientists (BRAINS) 1-R01MH104175, NIH-NIA 1R01AG048908-01A1, Ellison Medical Foundation New Scholar in Aging, Whitehall Foundation, Inscopix Decode award, Ellison Family Philanthropic support, Harvard Neurodiscovery Center/MADRC Center Pilot Grant Award, and HSCI Development grant. C.R. and P.D. were supported by HSCI Harvard Internship Program Award. We dedicate this manuscript to the late Dr. Joseph Altman who pioneered the field of adult hippocampal neurogenesis (Altman and Das, 1965).

Received: September 14, 2015
Revised: May 19, 2016
Accepted: August 1, 2016
Published: September 1, 2016

REFERENCES

Aimone, J.B., Deng, W., and Gage, F.H. (2011). Resolving new memories: a critical look at the dentate gyrus, adult neurogenesis, and pattern separation. Neuron *70*, 589–596.

Akers, K.G., Martinez-Canabal, A., Restivo, L., Yiu, A.P., De Cristofaro, A., Hsiang, H.L., Wheeler, A.L., Guskjolen, A., Niibori, Y., Shoji, H., et al. (2014). Hippocampal neurogenesis regulates forgetting during adulthood and infancy. Science *344*, 598–602.

Altman, J., and Das, G.D. (1965). Autoradiographic and histological evidence of postnatal hippocampal neurogenesis in rats. J. Comp. Neurol. *124*, 319–335.

Bakker, A., Kirwan, C.B., Miller, M., and Stark, C.E. (2008). Pattern separation in the human hippocampal CA3 and dentate gyrus. Science *319*, 1640–1642.

Bakker, A., Krauss, G.L., Albert, M.S., Speck, C.L., Jones, L.R., Stark, C.E., Yassa, M.A., Bassett, S.S., Shelton, A.L., and Gallagher, M. (2012). Reduction of hippocampal hyperactivity improves cognition in amnestic mild cognitive impairment. Neuron *74*, 467–474.

Bergami, M., Masserdotti, G., Temprana, S.G., Motori, E., Eriksson, T.M., Göbel, J., Yang, S.M., Conzelmann, K.K., Schinder, A.F., Götz, M., and Berninger, B. (2015). A critical period for experience-dependent remodeling of adult-born neuron connectivity. Neuron *85*, 710–717.

Besnard, A., and Sahay, A. (2016). Adult hippocampal neurogenesis, fear generalization, and stress. Neuropsychopharmacology *41*, 24–44.

Burghardt, N.S., Park, E.H., Hen, R., and Fenton, A.A. (2012). Adult-born hippocampal neurons promote cognitive flexibility in mice. Hippocampus *22*, 1795–1808.

Chancey, J.H., Poulsen, D.J., Wadiche, J.I., and Overstreet-Wadiche, L. (2014). Hilar mossy cells provide the first glutamatergic synapses to adult-born dentate granule cells. J. Neurosci. *34*, 2349–2354.

Clelland, C.D., Choi, M., Romberg, C., Clemenson, G.D., Jr., Fragniere, A., Tyers, P., Jessberger, S., Saksida, L.M., Barker, R.A., Gage, F.H., and Bussey, T.J. (2009). A functional role for adult hippocampal neurogenesis in spatial pattern separation. Science *325*, 210–213.

Deng, W., Mayford, M., and Gage, F.H. (2013). Selection of distinct populations of dentate granule cells in response to inputs as a mechanism for pattern separation in mice. eLife *2*, e00312.

Denny, C.A., Burghardt, N.S., Schachter, D.M., Hen, R., and Drew, M.R. (2012). 4- to 6-week-old adult-born hippocampal neurons influence novelty-evoked exploration and contextual fear conditioning. Hippocampus *22*, 1188–1201.

Deshpande, A., Bergami, M., Ghanem, A., Conzelmann, K.K., Lepier, A., Götz, M., and Berninger, B. (2013). Retrograde monosynaptic tracing reveals the temporal evolution of inputs onto new neurons in the adult dentate gyrus and olfactory bulb. Proc. Natl. Acad. Sci. USA *110*, E1152–E1161.

Encinas, J.M., and Sierra, A. (2012). Neural stem cell deforestation as the main force driving the age-related decline in adult hippocampal neurogenesis. Behav. Brain Res. *227*, 433–439.

Eriksson, P.S., Perfilieva, E., Björk-Eriksson, T., Alborn, A.M., Nordborg, C., Peterson, D.A., and Gage, F.H. (1998). Neurogenesis in the adult human hippocampus. Nat. Med. *4*, 1313–1317.

Foudi, A., Hochedlinger, K., Van Buren, D., Schindler, J.W., Jaenisch, R., Carey, V., and Hock, H. (2009). Analysis of histone 2B-GFP retention reveals slowly cycling hematopoietic stem cells. Nat. Biotechnol. *27*, 84–90.

Garthe, A., Behr, J., and Kempermann, G. (2009). Adult-generated hippocampal neurons allow the flexible use of spatially precise learning strategies. PLoS ONE *4*, e5464.

Ge, S., Yang, C.H., Hsu, K.S., Ming, G.L., and Song, H. (2007). A critical period for enhanced synaptic plasticity in newly generated neurons of the adult brain. Neuron *54*, 559–566.

Gilbert, P.E., Kesner, R.P., and Lee, I. (2001). Dissociating hippocampal subregions: double dissociation between dentate gyrus and CA1. Hippocampus *11*, 626–636.

Gracian, E.I., Shelley, L.E., Morris, A.M., and Gilbert, P.E. (2013). Age-related changes in place learning for adjacent and separate locations. Neurobiol. Aging *34*, 2304–2309.

Gu, Y., Arruda-Carvalho, M., Wang, J., Janoschka, S.R., Josselyn, S.A., Frankland, P.W., and Ge, S. (2012). Optical controlling reveals time-dependent roles for adult-born dentate granule cells. Nat. Neurosci. *15*, 1700–1706.

Guzowski, J.F., and Worley, P.F. (2001). Cellular compartment analysis of temporal activity by fluorescence in situ hybridization (catFISH). Curr. Protoc. Neurosci. *Chapter 1*, 8.

Hattiangady, B., and Shetty, A.K. (2008). Aging does not alter the number or phenotype of putative stem/progenitor cells in the neurogenic region of the hippocampus. Neurobiol. Aging *29*, 129–147.

Ikrar, T., Guo, N., He, K., Besnard, A., Levinson, S., Hill, A., Lee, H.K., Hen, R., Xu, X., and Sahay, A. (2013). Adult neurogenesis modifies excitability of the dentate gyrus. Front. Neural Circuits *7*, 204.

Jinde, S., Zsiros, V., Jiang, Z., Nakao, K., Pickel, J., Kohno, K., Belforte, J.E., and Nakazawa, K. (2012). Hilar mossy cell degeneration causes transient dentate granule cell hyperexcitability and impaired pattern separation. Neuron *76*, 1189–1200.

Jung, M.W., Wiener, S.I., and McNaughton, B.L. (1994). Comparison of spatial firing characteristics of units in dorsal and ventral hippocampus of the rat. J. Neurosci. *14*, 7347–7356.

Kempermann, G., Kuhn, H.G., and Gage, F.H. (1997). More hippocampal neurons in adult mice living in an enriched environment. Nature *386*, 493–495.

Kjelstrup, K.B., Solstad, T., Brun, V.H., Hafting, T., Leutgeb, S., Witter, M.P., Moser, E.I., and Moser, M.B. (2008). Finite scale of spatial representation in the hippocampus. Science *321*, 140–143.

Kropff, E., Yang, S.M., and Schinder, A.F. (2015). Dynamic role of adult-born dentate granule cells in memory processing. Curr. Opin. Neurobiol. *35*, 21–26.

Leutgeb, J.K., Leutgeb, S., Moser, M.B., and Moser, E.I. (2007). Pattern separation in the dentate gyrus and CA3 of the hippocampus. Science *315*, 961–966.

Lie, D.C., Colamarino, S.A., Song, H.J., Désiré, L., Mira, H., Consiglio, A., Lein, E.S., Jessberger, S., Lansford, H., Dearie, A.R., and Gage, F.H. (2005). Wnt signalling regulates adult hippocampal neurogenesis. Nature *437*, 1370–1375.

Lin, D., Boyle, M.P., Dollar, P., Lee, H., Lein, E.S., Perona, P., and Anderson, D.J. (2011). Functional identification of an aggression locus in the mouse hypothalamus. Nature *470*, 221–226.

Ma, D.K., Jang, M.H., Guo, J.U., Kitabatake, Y., Chang, M.L., Pow-Anpongkul, N., Flavell, R.A., Lu, B., Ming, G.L., and Song, H. (2009). Neuronal activity-induced Gadd45b promotes epigenetic DNA demethylation and adult neurogenesis. Science *323*, 1074–1077.

Marín-Burgin, A., Mongiat, L.A., Pardi, M.B., and Schinder, A.F. (2012). Unique processing during a period of high excitation/inhibition balance in adult-born neurons. Science *335*, 1238–1242.

McAvoy, K., Besnard, A., and Sahay, A. (2015a). Adult hippocampal neurogenesis and pattern separation in DG: a role for feedback inhibition in modulating sparseness to govern population-based coding. Front. Syst. Neurosci. *9*, 120.

McAvoy, K., Russo, C., Kim, S., Rankin, G., and Sahay, A. (2015b). Fluoxetine induces input-specific hippocampal dendritic spine remodeling along the septotemporal axis in adulthood and middle age. Hippocampus *25*, 1429–1446.

McNaughton, B., and Morris, R. (1987). Hippocampal synaptic enhancement and information storage within a distributed memory system. Trends Neurosci. *10*, 408–415.

Nakashiba, T., Cushman, J.D., Pelkey, K.A., Renaudineau, S., Buhl, D.L., McHugh, T.J., Rodriguez Barrera, V., Chittajallu, R., Iwamoto, K.S., McBain, C.J., et al. (2012). Young dentate granule cells mediate pattern separation, whereas old granule cells facilitate pattern completion. Cell *149*, 188–201.

Neunuebel, J.P., and Knierim, J.J. (2014). CA3 retrieves coherent representations from degraded input: direct evidence for CA3 pattern completion and dentate gyrus pattern separation. Neuron *81*, 416–427.

Niibori, Y., Yu, T.S., Epp, J.R., Akers, K.G., Josselyn, S.A., and Frankland, P.W. (2012). Suppression of adult neurogenesis impairs population coding of similar contexts in hippocampal CA3 region. Nat. Commun. *3*, 1253.

O'Reilly, R.C., and McClelland, J.L. (1994). Hippocampal conjunctive encoding, storage, and recall: avoiding a trade-off. Hippocampus *4*, 661–682.

Pan, Y.W., Chan, G.C., Kuo, C.T., Storm, D.R., and Xia, Z. (2012). Inhibition of adult neurogenesis by inducible and targeted deletion of ERK5 mitogen-activated protein kinase specifically in adult neurogenic regions impairs contextual fear extinction and remote fear memory. J. Neurosci. *32*, 6444–6455.

Restivo, L., Niibori, Y., Mercaldo, V., Josselyn, S.A., and Frankland, P.W. (2015). Development of adult-generated cell connectivity with excitatory and inhibitory cell populations in the hippocampus. J. Neurosci. *35*, 10600–10612.

Rolls, E.T., and Kesner, R.P. (2006). A computational theory of hippocampal function, and empirical tests of the theory. Prog. Neurobiol. *79*, 1–48.

Sahay, A., Scobie, K.N., Hill, A.S., O'Carroll, C.M., Kheirbek, M.A., Burghardt, N.S., Fenton, A.A., Dranovsky, A., and Hen, R. (2011a). Increasing adult hippocampal neurogenesis is sufficient to improve pattern separation. Nature *472*, 466–470.

Sahay, A., Wilson, D.A., and Hen, R. (2011b). Pattern separation: a common function for new neurons in hippocampus and olfactory bulb. Neuron *70*, 582–588.

Satvat, E., Schmidt, B., Argraves, M., Marrone, D.F., and Markus, E.J. (2011). Changes in task demands alter the pattern of zif268 expression in the dentate gyrus. J. Neurosci. *31*, 7163–7167.

Saxe, M.D., Battaglia, F., Wang, J.W., Malleret, G., David, D.J., Monckton, J.E., Garcia, A.D., Sofroniew, M.V., Kandel, E.R., Santarelli, L., et al. (2006). Ablation of hippocampal neurogenesis impairs contextual fear conditioning and synaptic plasticity in the dentate gyrus. Proc. Natl. Acad. Sci. USA *103*, 17501–17506.

Schmidt-Hieber, C., Jonas, P., and Bischofberger, J. (2004). Enhanced synaptic plasticity in newly generated granule cells of the adult hippocampus. Nature *429*, 184–187.

Scobie, K.N., Hall, B.J., Wilke, S.A., Klemenhagen, K.C., Fujii-Kuriyama, Y., Ghosh, A., Hen, R., and Sahay, A. (2009). Krüppel-like factor 9 is necessary for late-phase neuronal maturation in the developing dentate gyrus and during adult hippocampal neurogenesis. J. Neurosci. *29*, 9875–9887.

Small, S.A., Schobel, S.A., Buxton, R.B., Witter, M.P., and Barnes, C.A. (2011). A pathophysiological framework of hippocampal dysfunction in ageing and disease. Nat. Rev. Neurosci. *12*, 585–601.

Snyder, J.S., Kee, N., and Wojtowicz, J.M. (2001). Effects of adult neurogenesis on synaptic plasticity in the rat dentate gyrus. J. Neurophysiol. *85*, 2423–2431.

Snyder, J.S., Choe, J.S., Clifford, M.A., Jeurling, S.I., Hurley, P., Brown, A., Kamhi, J.F., and Cameron, H.A. (2009). Adult-born hippocampal neurons are more numerous, faster maturing, and more involved in behavior in rats than in mice. J. Neurosci. *29*, 14484–14495.

Song, J., Zhong, C., Bonaguidi, M.A., Sun, G.J., Hsu, D., Gu, Y., Meletis, K., Huang, Z.J., Ge, S., Enikolopov, G., et al. (2012). Neuronal circuitry mechanism regulating adult quiescent neural stem-cell fate decision. Nature *489*, 150–154.

Spalding, K.L., Bergmann, O., Alkass, K., Bernard, S., Salehpour, M., Huttner, H.B., Boström, E., Westerlund, I., Vial, C., Buchholz, B.A., et al. (2013). Dynamics of hippocampal neurogenesis in adult humans. Cell *153*, 1219–1227.

Stone, S.S., Teixeira, C.M., Zaslavsky, K., Wheeler, A.L., Martinez-Canabal, A., Wang, A.H., Sakaguchi, M., Lozano, A.M., and Frankland, P.W. (2011). Functional convergence of developmentally and adult-generated granule cells in dentate gyrus circuits supporting hippocampus-dependent memory. Hippocampus *21*, 1348–1362.

Swan, A.A., Clutton, J.E., Chary, P.K., Cook, S.G., Liu, G.G., and Drew, M.R. (2014). Characterization of the role of adult neurogenesis in touch-screen discrimination learning. Hippocampus *24*, 1581–1591.

Tada, T., and Sheng, M. (2006). Molecular mechanisms of dendritic spine morphogenesis. Curr. Opin. Neurobiol. *16*, 95–101.

Tashiro, A., Sandler, V.M., Toni, N., Zhao, C., and Gage, F.H. (2006). NMDA-receptor-mediated, cell-specific integration of new neurons in adult dentate gyrus. Nature *442*, 929–933.

Tashiro, A., Makino, H., and Gage, F.H. (2007). Experience-specific functional modification of the dentate gyrus through adult neurogenesis: a critical period during an immature stage. J. Neurosci. *27*, 3252–3259.

Temprana, S.G., Mongiat, L.A., Yang, S.M., Trinchero, M.F., Alvarez, D.D., Kropff, E., Giacomini, D., Beltramone, N., Lanuza, G.M., and Schinder, A.F. (2015). Delayed coupling to feedback inhibition during a critical period for the integration of adult-born granule cells. Neuron *85*, 116–130.

Toner, C.K., Pirogovsky, E., Kirwan, C.B., and Gilbert, P.E. (2009). Visual object pattern separation deficits in nondemented older adults. Learn. Mem. *16*, 338–342.

Toni, N., Teng, E.M., Bushong, E.A., Aimone, J.B., Zhao, C., Consiglio, A., van Praag, H., Martone, M.E., Ellisman, M.H., and Gage, F.H. (2007). Synapse formation on neurons born in the adult hippocampus. Nat. Neurosci. *10*, 727–734.

Tronel, S., Belnoue, L., Grosjean, N., Revest, J.M., Piazza, P.V., Koehl, M., and Abrous, D.N. (2012). Adult-born neurons are necessary for extended contextual discrimination. Hippocampus *22*, 292–298.

van Praag, H., Kempermann, G., and Gage, F.H. (2000). Neural consequences of environmental enrichment. Nat. Rev. Neurosci. *1*, 191–198.

Villeda, S.A., Luo, J., Mosher, K.I., Zou, B., Britschgi, M., Bieri, G., Stan, T.M., Fainberg, N., Ding, Z., Eggel, A., et al. (2011). The ageing systemic milieu negatively regulates neurogenesis and cognitive function. Nature *477*, 90–94.

Vivar, C., Potter, M.C., Choi, J., Lee, J.Y., Stringer, T.P., Callaway, E.M., Gage, F.H., Suh, H., and van Praag, H. (2012). Monosynaptic inputs to new neurons in the dentate gyrus. Nat. Commun. *3*, 1107.

Vivar, C., Peterson, B.D., and van Praag, H. (2016). Running rewires the neuronal network of adult-born dentate granule cells. Neuroimage *131*, 29–41.

Vukovic, J., Borlikova, G.G., Ruitenberg, M.J., Robinson, G.J., Sullivan, R.K., Walker, T.L., and Bartlett, P.F. (2013). Immature doublecortin-positive hippocampal neurons are important for learning but not for remembering. J. Neurosci. *33*, 6603–6613.

Vuksic, M., Del Turco, D., Bas Orth, C., Burbach, G.J., Feng, G., Müller, C.M., Schwarzacher, S.W., and Deller, T. (2008). 3D-reconstruction and functional properties of GFP-positive and GFP-negative granule cells in the fascia dentata of the Thy1-GFP mouse. Hippocampus *18*, 364–375.

Wickersham, I.R., Lyon, D.C., Barnard, R.J., Mori, T., Finke, S., Conzelmann, K.K., Young, J.A., and Callaway, E.M. (2007). Monosynaptic restriction of transsynaptic tracing from single, genetically targeted neurons. Neuron *53*, 639–647.

Wojtowicz, J.M., Askew, M.L., and Winocur, G. (2008). The effects of running and of inhibiting adult neurogenesis on learning and memory in rats. Eur. J. Neurosci. *27*, 1494–1502.

Wu, M.V., Luna, V.M., and Hen, R. (2015). Running rescues a fear-based contextual discrimination deficit in aged mice. Front. Syst. Neurosci. *9*, 114.

Yassa, M.A., and Stark, C.E. (2011). Pattern separation in the hippocampus. Trends Neurosci. *34*, 515–525.

Yassa, M.A., Stark, S.M., Bakker, A., Albert, M.S., Gallagher, M., and Stark, C.E. (2010). High-resolution structural and functional MRI of hippocampal CA3 and dentate gyrus in patients with amnestic Mild Cognitive Impairment. Neuroimage *51*, 1242–1252.

Yassa, M.A., Mattfeld, A.T., Stark, S.M., and Stark, C.E. (2011). Age-related memory deficits linked to circuit-specific disruptions in the hippocampus. Proc. Natl. Acad. Sci. USA *108*, 8873–8878.

Zhu, P., Aller, M.I., Baron, U., Cambridge, S., Bausen, M., Herb, J., Sawinski, J., Cetin, A., Osten, P., Nelson, M.L., et al. (2007). Silencing and un-silencing of tetracycline-controlled genes in neurons. PLoS ONE *2*, e533.

Neuron, Volume *91*

Supplemental Information

Modulating Neuronal Competition Dynamics in the Dentate Gyrus to Rejuvenate Aging Memory Circuits

Kathleen M. McAvoy, Kimberly N. Scobie, Stefan Berger, Craig Russo, Nannan Guo, Pakanat Decharatanachart, Hugo Vega-Ramirez, Sam Miake-Lye, Michael Whalen, Mark Nelson, Matteo Bergami, Dusan Bartsch, Rene Hen, Benedikt Berninger, and Amar Sahay

Supplementary Figures

Supplementary Figure 1. Characterization of *mDG rtTA*-dependent transactivation patterns of different tetO-linked transgenes

(Corresponds to Main Figure 1)

A) Schematic of genetic strategy to inducibly and reversibly overexpress *Klf9*. (B) Representative micrographs of *Klf9* in situ hybridization showing expression in regions quantified in Figure 1D. Within the DG, *Klf9* overexpression and reporter expression was restricted to the granule cell layer (GCL) and absent from mossy cells or hilar interneurons.

C, D) A triple transgenic strategy generates DG-restricted expression. (C) Schematic of triple transgenic design used in D. (D) Sagittal section of triple transgenic *mDG* $^{tetO\text{-}Cre/+;\ floxed\ STOP\ LacZ/+}$ showing DG restricted expression by Beta-Galactosidase staining.

E, F) *mDG* rtTA drives expression of tetO-linked transgenes in forebrain. (E) Schematic of genetic strategy used in F. (F) Representative coronal hemisections showing immunohistochemical labeling for Beta-Galactosidase in *mDG* $^{teto\text{-}TauLacZ/+}$ mice in hippocampus. Scale bars 100μm (B), 500μm (D, F).

Figure S1

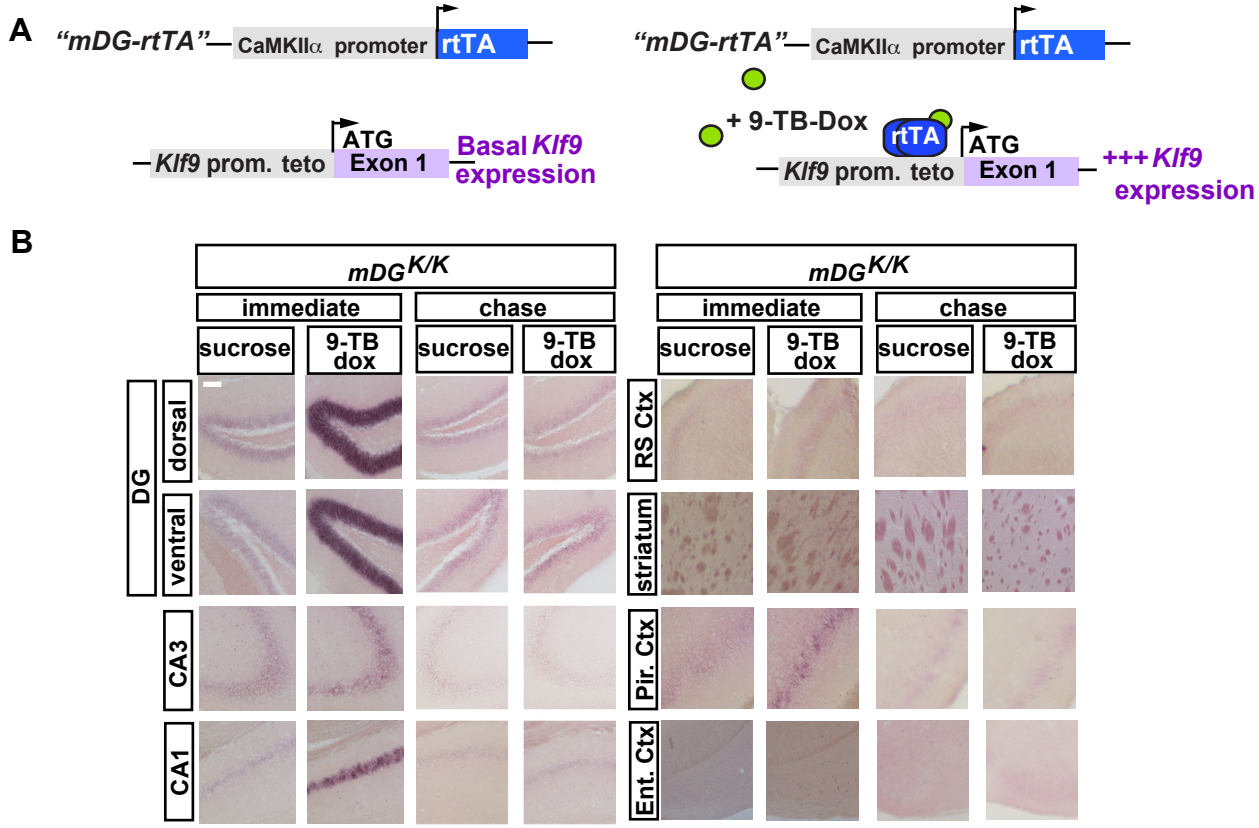
A
"mDG-rtTA"
CaMKIIα promoter
rtTA
Klf9 prom. teto
ATG
Exon 1
Basal Klf9 expression
+ 9-TB-Dox
+++ Klf9 expression
B
mDG K/K
immediate
chase
sucrose
9-TB dox
DG
dorsal
ventral
CA3
CA1
RS Ctx
striatum
Pir. Ctx
Ent. Ctx
C
teto
CRE
ROSA f.STOP
LacZ
D
mDG teto-Cre/+;floxed-STOPLacZ/+
B-gal stain
E
TauLacZ
F
mDG tetoK/+;tetoTauLacZ
α-B-gal

Supplementary Figure 2. Characterization of c-fos expression, dendritic spine density in striatum and retrosplenial cortex, and cell death in *mDG* $^{K/K}$ mice (Corresponds to Main Figure 2)

A, B) *mDG* $^{K/K}$ mice show decreased c-fos activation in the hippocampus immediately following two weeks of 9TBD treatment in drinking water in A) naïve or B) open field (30 min.) exposed mice (see Figure 2I for quantification).

C,D) At the chase timepoint (two weeks of treatment, followed by two weeks chase) c-fos immunohistochemistry reveals no change in activity in hippocampal regions in 9TBD-treated *mDG* $^{K/K}$ mice that were C) naïve or D) exposed to 30 minutes of open field (see Figure 2J for quantification).

E) c-fos activation in striatum of vehicle- and 9-TBD-treated *mDG* $^{K/K}$ mice following 30 minutes of open field exploration at the chase timepoint is similar (n=3,3).

F) *Klf9* overexpression in mature DGCs does not affect IML dendritic spine density. Maximum intensity projection images of confocal z-stack scans of IML dendritic segments of *mDG* $^{K/K;\ Thy1\text{-}GFP/+}$ mice at the immediate timepoint (two weeks of vehicle or 9TBD). Quantification of spine density in the IML (n=4,3, right).

G) 9TBD and vehicle-treated *mDG* $^{K/K}$ mice at chase timepoint have similar dendritic spine densities in AAV_9-CaMKIIα-GFP-labeled striatal neurons or Retrosplenial cortex neurons (n=3,3).

H) Top: representative images of cleaved caspase-3 immunolabled cells in the granule cell layer of 9BTD or vehicle-treated *mDG* $^{K/K}$ mice and wild-type mice 24 hours post-irradiation (tissue kind gift of Dr. David Scadden). Below: Klf9 overexpression does not change the number of dying (cleaved caspase-3+) cells in the DG. Scale bar: 50μm (A-D), 2μm (F), 100μm top, 2μm below (G). Data represent mean ± SEM.

Figure S2

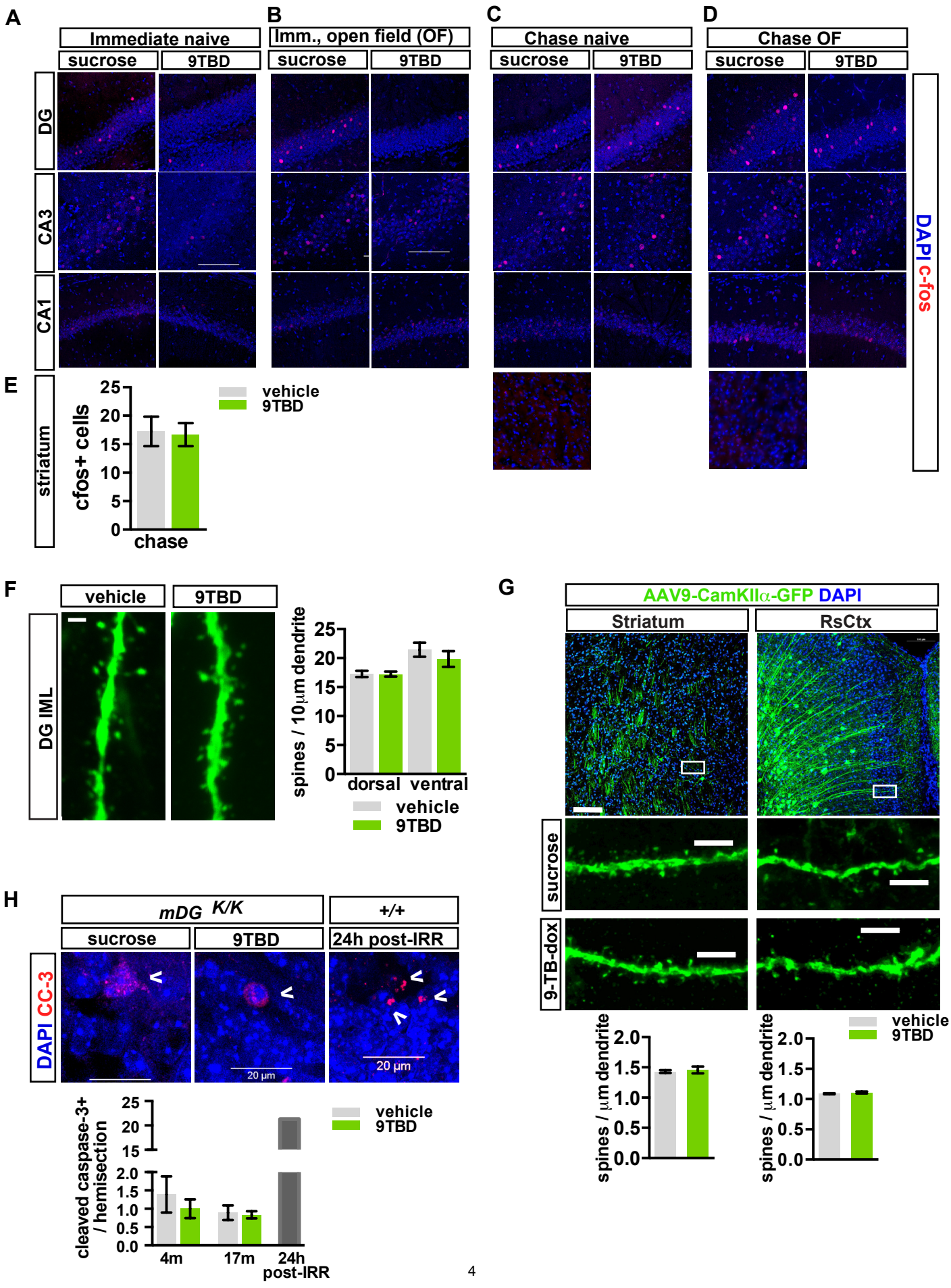
A
Immediate naive
sucrose
9TBD
B
Imm., open field (OF)
sucrose
9TBD
C
Chase naive
sucrose
9TBD
D
Chase OF
sucrose
9TBD
DG
CA3
CA1
DAPI c-fos
E
striatum
cfos+ cells
25
20
15
10
5
0
chase
vehicle
9TBD
F
vehicle
9TBD
DG IML
spines / 10 μm dendrite
25
20
15
10
5
0
dorsal
ventral
vehicle
9TBD
G
AAV9-CamKIIα-GFP DAPI
Striatum
RsCtx
sucrose
9-TB-dox
spines / μm dendrite
2.0
1.5
1.0
0.5
0.0
vehicle
9TBD
H
mDG K/K
+/+
sucrose
9TBD
24h post-IRR
DAPI CC-3
20 μm
cleaved caspase-3+ / hemisection
25
20
15
2.0
1.5
1.0
0.5
0.0
4m
17m
24h post-IRR
vehicle
9TBD

Supplementary Figure 3. Genotype X Treatment enhances adult hippocampal neurogenesis but not olfactory bulb neurogenesis
(Corresponds to Main Figure 3)

A, B) *Klf9* overexpression in mature DGCs affects the survival of adult-born cells of specific ages. Schematic of injection paradigm showing the timing of injection (i.p.) of different thymidine analogs in separate cohorts of *mDG* $^{K/K}$ mice. Representative micrographs of the upper blade of the DG showing BrdU (-3w), CldU (-2w), and IdU (0w) positive cells. (B) Quantification of XdU+ cells per DG: BrdU (-3w, n=4,4, p=0.239), CldU (-2w, n=4,3 p=0.0136), and IdU (0w, n=3,3 p=0.0249).

C, D) Increases in DCX+ numbers and survival of 3 week-old adult-born cells require both genotype (*mDG* $^{K/K}$) and treatment (9TBD). Representative images of BrdU labeling in the upper blade of the DG and DCX labeling in the dorsal DG of *K/K* mice immediately following treatment with sucrose or 9TBD and *mDG* $^{K/K}$ mice treated with 9TBD. (D) Quantification of BrdU positive cells (n=4 [*K/K*, vehicle], 3 [*K/K*, 9TBD], 3 [*mDG* $^{K/K}$ 9TBD], ANOVA F=43.58 p<0.0001, *K/K* vehicle, *K/K* 9TBD vs. *mDG* $^{K/K}$ 9TBD p<0.05). Quantification of DCX positive cells per dorsal DG section (n=4 [*K/K*, vehicle], 3 [*K/K*, 9TBD], 3 [*mDG* $^{K/K}$ 9TBD], ANOVA F=33.66 p<0.0001, *K/K* vehicle, *K/K* 9TBD vs. *mDG* $^{K/K}$ 9TBD p<0.05).

E - G) *Klf9* overexpression in *mDG* $^{K/K}$ mice does not affect SVZ neurogenesis. (E) Representative images showing DCX labeling in the SVZ of *K/K* mice and *mDG* $^{K/+}$ mice immediately after two weeks 9TBD treatment. Quantification of DCX+ neurons in SVZ (right, n=4, 3). (E1-E4) Boxes correspond to high magnification images of DCX+ cells in SVZ (E1 and E2) (F) Representative images of proliferation in the SVZ. BrdU labeled cells in the SVZ 2 hours after BrdU injection in *mDG* $^{K/K}$ mice immediately after two weeks treatment with vehicle or 9TBD. Quantification and schematic showing the timing of BrdU injection (right, n=12,10). (G) Images of BrdU positive cells in the MOB of *mDG* $^{K/K}$ mice treated with vehicle or 9TBD. Quantification and schematic showing the timing of BrdU injection (right, n=3,3). Scale bar: 20μm (A), 20μm, 100μm (C), 500μm (E), 500μm (F), 20μm (G). ***p<0.001, **p<0.01, *p<0.05. Data represent mean ± SEM.

Figure S3

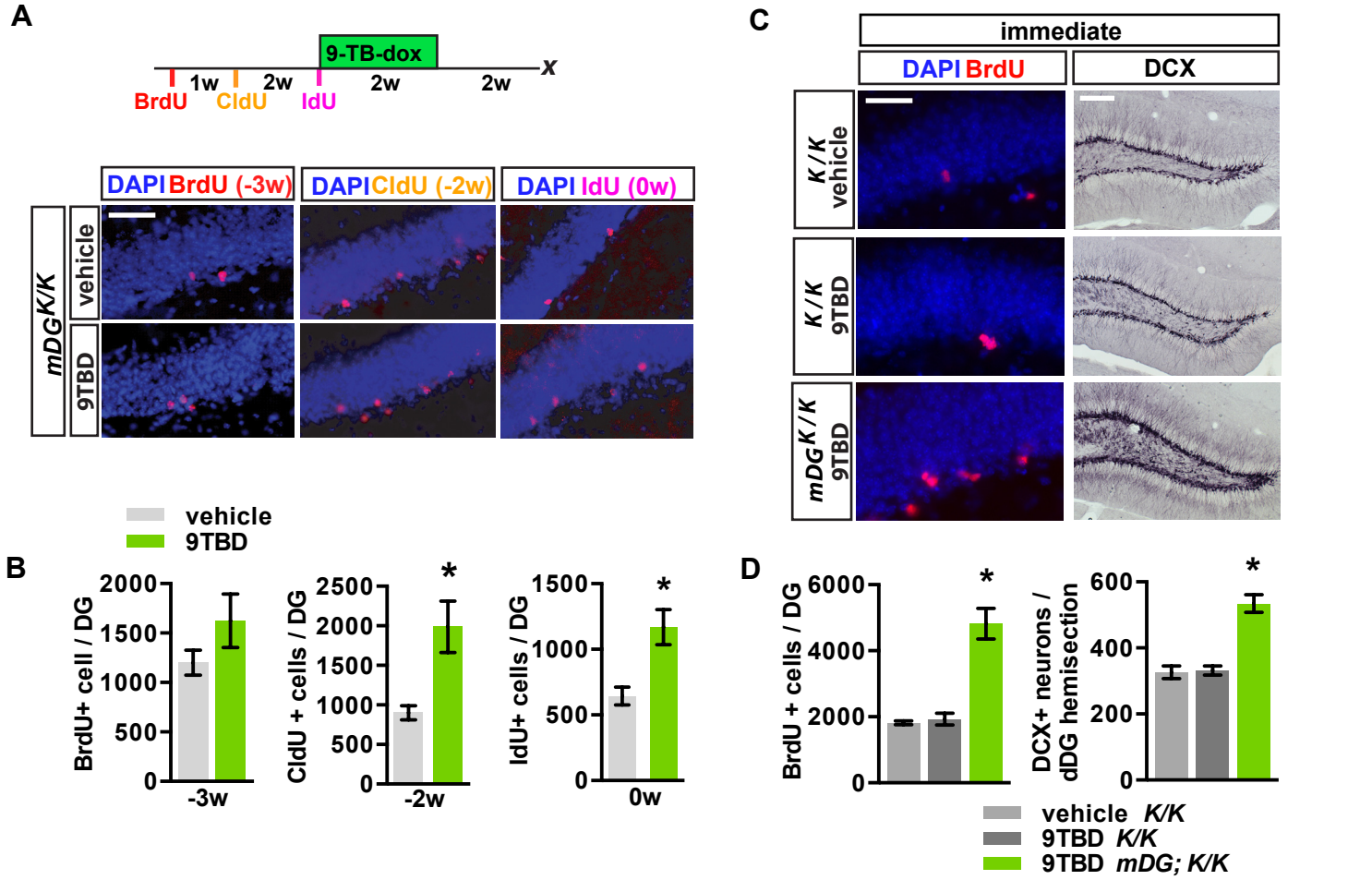
A
9-TB-dox
BrdU
1w
CldU
2w
IdU
2w
2w
x
DAPI BrdU (-3w)
DAPI CldU (-2w)
DAPI IdU (0w)
mDGK/K
vehicle
9TBD
C
immediate
DAPI BrdU
DCX
K/K vehicle
K/K 9TBD
mDGK/K 9TBD
vehicle
9TBD
B
BrdU+ cell / DG
CldU + cells / DG
IdU+ cells / DG
-3w
-2w
0w
D
BrdU + cells / DG
DCX+ neurons / dDG hemisection
vehicle K/K
9TBD K/K
9TBD mDG; K/K
E
DCX
K/K 9TBD
mDG K/+ 9TBD
E1
E2
E3
E4
3 mos.
veh. / 9TBD
2w
SVZ DCX+ cells / hemisection
K/K
mDG K/+
F
SVZ
DAPI BrdU
mDG K/K vehicle
mDG K/K 9TBD
3 mos.
veh. / 9TBD
1w
1w
BrdU
SVZ BrdU+ cells / hemisection
G
MOB
BrdU
3 mos.
veh. / 9TBD
1w
1w
BrdU
2w
BrdU+ cells / image
vehicle
9TBD

Supplementary Figure 4. Analysis of cell fate specification and dendritic complexity, spine density and mossy fiber terminals of adult-born DGCs in *mDG* $^{K/K}$ mice

(Corresponds to Main Figure 5)

A, B) *Klf9* overexpression in mature DGCs does not affect adult-born cell fate specification. (A) Schematic showing timing of BrdU injection and 9TBD administration. Representative confocal images adult-born cells (NeuN+BrdU+, GFAP+BrdU+) in DG. Box indicates image in outlined in gray below. (B) 79.5±5.1% and 85.9±2.4% of 5 week-old BrdU-positive population labeled for NeuN and 5.7±1.7% and 6.1±1.4% labeled for GFAP in vehicle and 9TBD treated mice, respectively.

C-E) *Klf9* overexpression in mature DGCs does not affect adult-born DGC morphology. (C) Schematic showing timing of retroviral injections used in D,E to quantify MFTs from 5 week-old adult-born DGCs labeled with Tdtomato. Representative images of 5 week-old adult-born DGCs and MFTs labeled with TdTomato. (D) MFTs of 5 week-old adult-born DGCs of 9TBD treated *K/K* or *mDG* $^{K/K}$ mice have comparable number of filopodia (n=5,5). Graph displays the percentage of imaged MFTs as function of filopodia number. (E) MFTs of 5 week-old adult-born DGCs of 9TBD treated *K/K* or *mDG* $^{K/K}$ mice are similar in size. Graph displays the percentage distribution of the area of imaged MFTs (n=5,5).

F - I) Scholl analysis reveals that there are no morphological differences between vehicle and 9TBD treated 4-week or 6-week old neurons. (F) Representative maximum intensity projections of Z-stacks of 4 and 6 week old vehicle or 9TBD-treated *mDG* $^{K/K}$ mice. There are no differences in (G) total dendritic length, (H) maximum branch number, or (I) Scholl analysis of branching morphology between 4-week or 6-week-old neurons from vehicle and 9TBD-treated *mDG* $^{K/K}$ mice (n=5 for all groups, with 5-10 neurons per animal). Scale bar: 100μm (A), 500μm, 2μm right (C), 20μm (F). Data represent mean ± SEM.

Figure S4

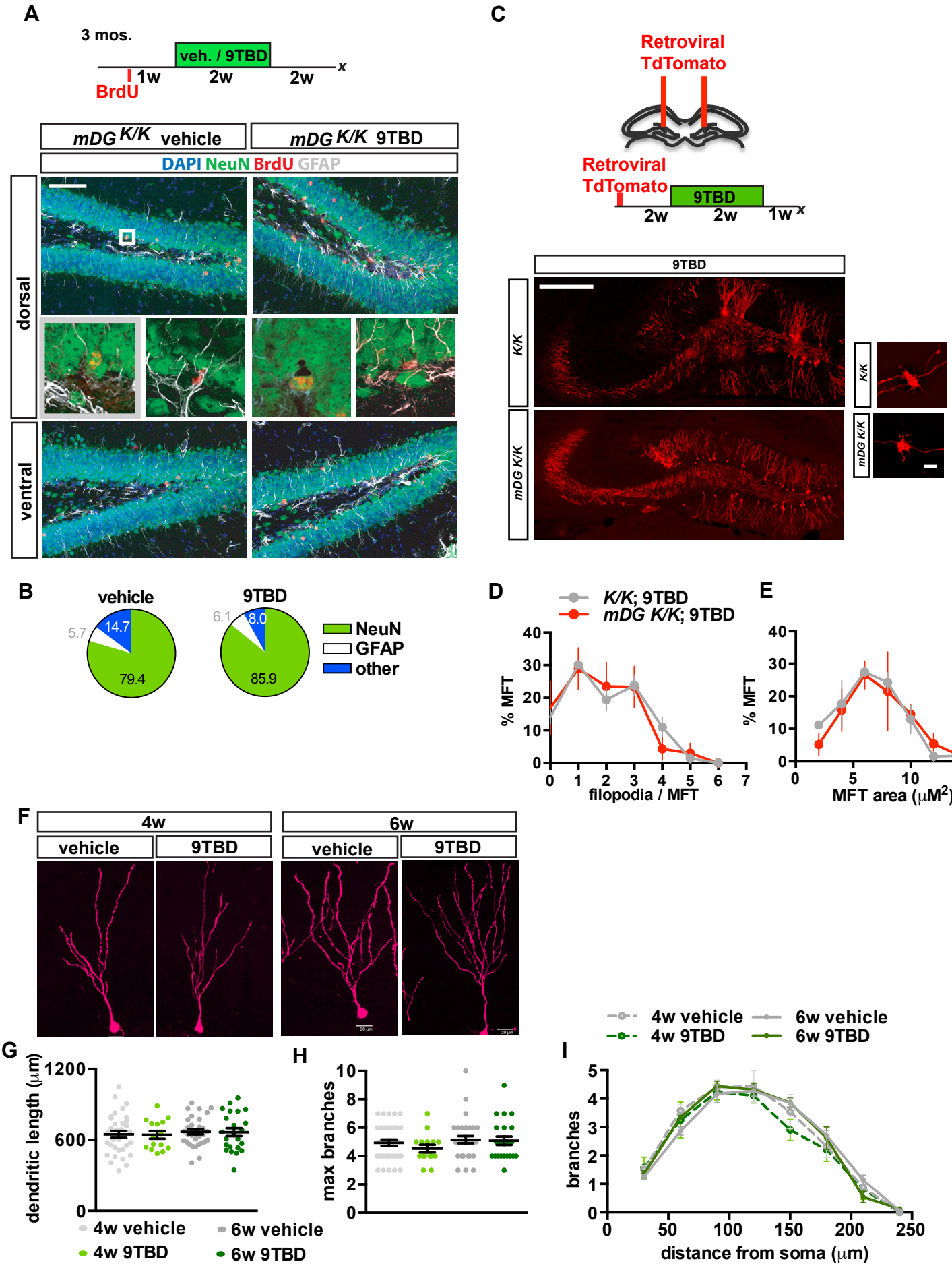
A
3 mos.
veh. / 9TBD
BrdU
1w
2w
2w
x
mDG K/K vehicle
mDG K/K 9TBD
DAPI NeuN BrdU GFAP
dorsal
ventral
C
Retroviral
TdTomato
Retroviral
TdTomato
9TBD
2w
2w
1w
x
9TBD
K/K
mDG K/K
K/K
mDG K/K
B
vehicle
9TBD
5.7
14.7
79.4
6.1
8.0
85.9
NeuN
GFAP
other
D
K/K; 9TBD
mDG K/K; 9TBD
% MFT
filopodia / MFT
E
% MFT
MFT area (μM2)
F
4w
6w
vehicle
9TBD
vehicle
9TBD
G
dendritic length (μm)
4w vehicle
6w vehicle
4w 9TBD
6w 9TBD
H
max branches
I
4w vehicle
6w vehicle
4w 9TBD
6w 9TBD
branches
distance from soma (μm)

Supplementary Figure 5. Genetic expansion of adult-born DGCs or genetic overexpression of *Klf9* in CA1 does not affect innate anxiety and spatial reversal learning, respectively

(Corresponds to Main Figure 6)

A) Schematic of behavioral testing regimen of adult *mDG* $^{K/K}$ mice (n=9, 9 except where indicated).

B) Vehicle and 9TBD treated *mDG* $^{K/K}$ mice exhibited comparable levels of locomotor activity (B') (ANOVA, time: $F_{(11,176)}$=16.78, p<0.0001, treatment: $F_{(1,16)}$=0.005, p=0.9453, interaction: $F_{(11,176)}$=1.187, p=0.2989), rearing behaviors (B'') (p=0.5419), and distance traveled in the periphery or center of the open field (B''') (center, p=0.7339) over 60 minutes.

C) Vehicle and 9TBD treated *mDG* $^{K/K}$ mice traveled comparable distances in the light and dark compartments over 10 minutes (% distance in light, p=0.4712).

D) Vehicle and 9TBD treated *mDG* $^{K/K}$ mice spent comparable time in the open and closed arms of elevated plus maze over 5 minutes (n=14,14 time open arms p=0.2729).

E) Vehicle and 9TBD treated *mDG* $^{K/K}$ mice spent comparable time immobile on day 1 (p=0.6564) and day 2 (p=0.913) of the forced swim test.

F) 9TBD treated *mDG* $^{K/K}$ mice spent more time interacting with the novel object in the test session immediately following three training sessions (n=8,8) (ANOVA, object: $F_{(1,12)}$=7.753, p=0.0165, treatment: $F_{(1,12)}$=10.91, p=0.0063, interaction: $F_{(1,12)}$=1.866, p=0.197).

G) Schematic of behavioral testing regimen of 16 month-old *mDG* $^{K/K}$ mice (n=9,9).

H) Vehicle and 9TBD treated 16 month-old *mDG* $^{K/K}$ mice traveled comparable distances in the light and dark compartments over 10 minutes (% distance in light, p=0.8616).

I) Vehicle and 9TBD treated 16 month-old *mDG* $^{K/K}$ mice exhibited comparable levels of locomotor activity (I) (ANOVA, time: $F_{(11,176)}$=8.519, p<0.0001, treatment: $F_{(1,16)}$=0.3773, p=0.5476, interaction: $F_{(11,176)}$=0.9137, p=0.5285), rearing behaviors (p=0.4540), and distance traveled in the periphery or center of the open field (% distance center, p=0.4289) over 60 minutes.

J - L) Local infusion of 9TBD in *mDG* $^{K/K}$ mice results in CA1-specific overexpression of *Klf9*. (J) schematic of local 9TBD infusion and testing paradigm. (K) Representative images showing CA1 overexpression of *Klf9*. (L) *Klf9* expression is increased in CA1,

but not DG, following 10 days of local 9TBD infusion (n=3,3, t-test CA1 p=0.0062 DG p=0.5343).

(M - Q) MWM analysis of mice two weeks post-CA1- *Klf9* overexpression reveals no differences in spatial learning, memory, or cognitive flexibility (n=9,9). (M) Both vehicle and 9TBD-treated mice show similar latency to reach the platform and (N) showed similar accurate performance on the initial hidden probe test (ANOVA, vehicle: F=30.07, p<0.0001, target v left, right, opposite p<0.05, 9TBD: F=11.50, p=0.0003, target v left, right, opposite p<0.05). (O) Vehicle and 9TBD-treated mice show no differences in latency to locate the reverse hidden platform location. (P) Both groups failed to prefer the new target quadrant on reversal day 3, whereas (Q) both groups showed a similar accurate preference for the target quadrant on reversal day 5 (ANOVA, vehicle: F=5.054, p=0.0259, target v left, opposite p<0.05, 9TBD: F=4.523, p=0.0488, target v right, opposite p<0.05). *p<0.05. Data represent mean ± SEM.

Figure S5

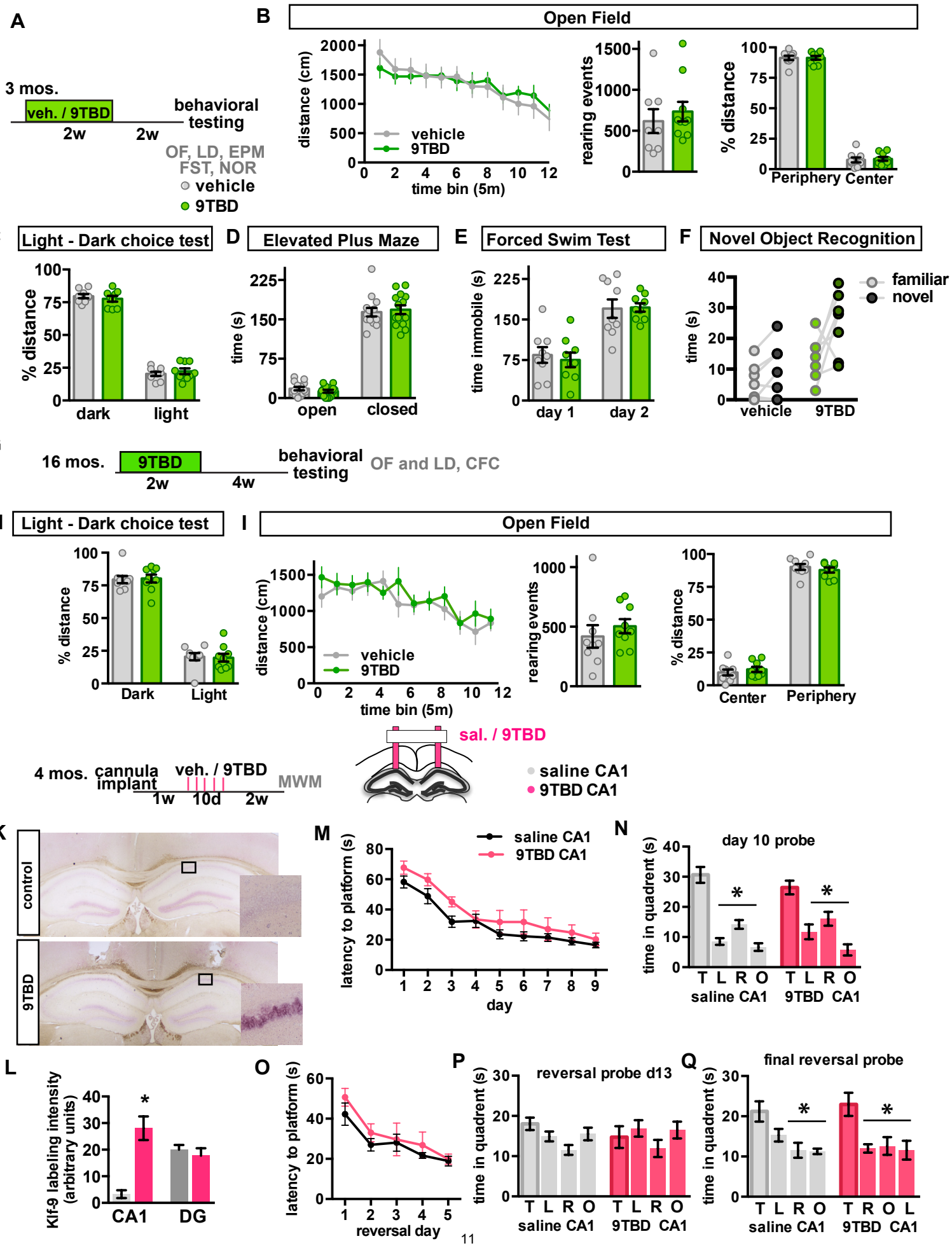
A
3 mos.
veh. / 9TBD
2w
2w
behavioral testing
OF, LD, EPM
FST, NOR
vehicle
9TBD
B
Open Field
distance (cm)
time bin (5m)
vehicle
9TBD
rearing events
% distance
Periphery
Center
C
Light - Dark choice test
% distance
dark
light
D
Elevated Plus Maze
time (s)
open
closed
E
Forced Swim Test
time immobile (s)
day 1
day 2
F
Novel Object Recognition
time (s)
familiar
novel
vehicle
9TBD
G
16 mos.
9TBD
2w
4w
behavioral testing
OF and LD, CFC
H
Light - Dark choice test
% distance
Dark
Light
I
Open Field
distance (cm)
time bin (5m)
vehicle
9TBD
rearing events
% distance
Center
Periphery
J
4 mos.
cannula implant
veh. / 9TBD
1w
10d
2w
MWM
sal. / 9TBD
saline CA1
9TBD CA1
K
control
9TBD
M
saline CA1
9TBD CA1
latency to platform (s)
day
N
day 10 probe
time in quadrent (s)
T L R O
saline CA1
T L R O
9TBD CA1
L
Klf-9 labeling intensity (arbitrary units)
CA1
DG
O
latency to platform (s)
reversal day
P
reversal probe d13
time in quadrent (s)
T L R O
saline CA1
T L R O
9TBD CA1
Q
final reversal probe
time in quadrent (s)
T L R O
saline CA1
T R O L
9TBD CA1

Supplementary Figure 6. Competence of NSC activation and modulation of neuronal competition dynamics is maintained following reinduction of *Klf9* overexpression in mature DGCs
(Corresponds to Main Figure 7)

A, B) *In situ* hybridization showing that *Klf9* transcripts are upregulated in the DG of 11 month- old *mDG*$^{K/K}$ mice immediately following treatment with 9TBD. (A) Representative images. (B) Quantification of *Klf9* expression (arbitrary units) in forebrain at the immediate and chase timepoints (n=7 [vehicle], 4 [immediate], 3 [chase], ANOVA, F=19.18 p=0.0005, vehicle vs. 9TBD immediate DG p<0.05)

C - E) Inducible *Klf9* overexpression in mature DGCs increases proliferation in 11 months old *mDG*$^{K/K}$ mice. (C) Representative Images. (D) Inducible *Klf9* overexpression in mature DGCs increases the Tbr2+ population in 11 months old *mDG*$^{K/K}$ mice (n=3,4, t-test, vehicle vs. dox p<0.0001). (E) Inducible *Klf9* overexpression in mature DGCs increases the MCM2+ population in 11 months old *mDG*$^{K/K}$ mice (n=3,4, t-test vehicle vs. dox immediate, p=0.0112).

F - L) Re-induction of *Klf-9* overexpression. (F) Schematic of experimental design for assessing the impact of re-induction of *Klf9* overexpression in mature DGCs on adult hippocampal neurogenesis in G – L (n=4 [V-V], 3 [D-V], 4[V-D], 4[D-D]). (G) *In situ* hybridization showing that *Klf9* transcripts are upregulated following multiple treatments with 9TBD. (H) Quantification of *Klf-9* expression (arbitrary units) in forebrain following first or second exposure to 9TBD (ANOVA DG: f=18.91 p=0.0002 V-V vs. V-D, D-D p<0.05, CA3: F=5.212 p=0.0201 V-V vs. D-D p<0.05, CA1: F=15.17 p=0.0005 V-V vs. V-D, D-D p<0.05, PC F=6.674 p=0.0094 V-V vs. V-D, D-D p<0.05). (I) Competence of NSC and progenitor activation is maintained following re-induction of *Klf9* overexpression. Representative images of Tbr2, MCM2, and Nestin-MCM2 labeling following first or second exposure to 9TBD. (J) Repeated inducible *Klf9* overexpression in mature DGCs produces comparable increases in the (J) DCX+ population, (K) Tbr2+ (ANOVA F=20.26 p<0.0001, V-V vs. V-D, D-D p<0.05), MCM2+ (ANOVA F=36.11 p<0.0001, V-V vs. V-D, D-D p<0.05) and DCX+ (ANOVA F=23.3 p<0.0001, V-V vs. V-D, D-D p<0.05) populations in the DG, as well as (L) comparable increases in activation of NSCs in the DG (ANOVA F=10.57 p=0.0014, V-V vs. V-D, D-D p<0.05). Scale bar: 500μm (A,G), 20μm (C,I), 50 μm (I, Nestin MCM2) 100μm (J). ***p<0.001, **p<0.01, *p<0.05. Data represent mean ± SEM.

Figure S6

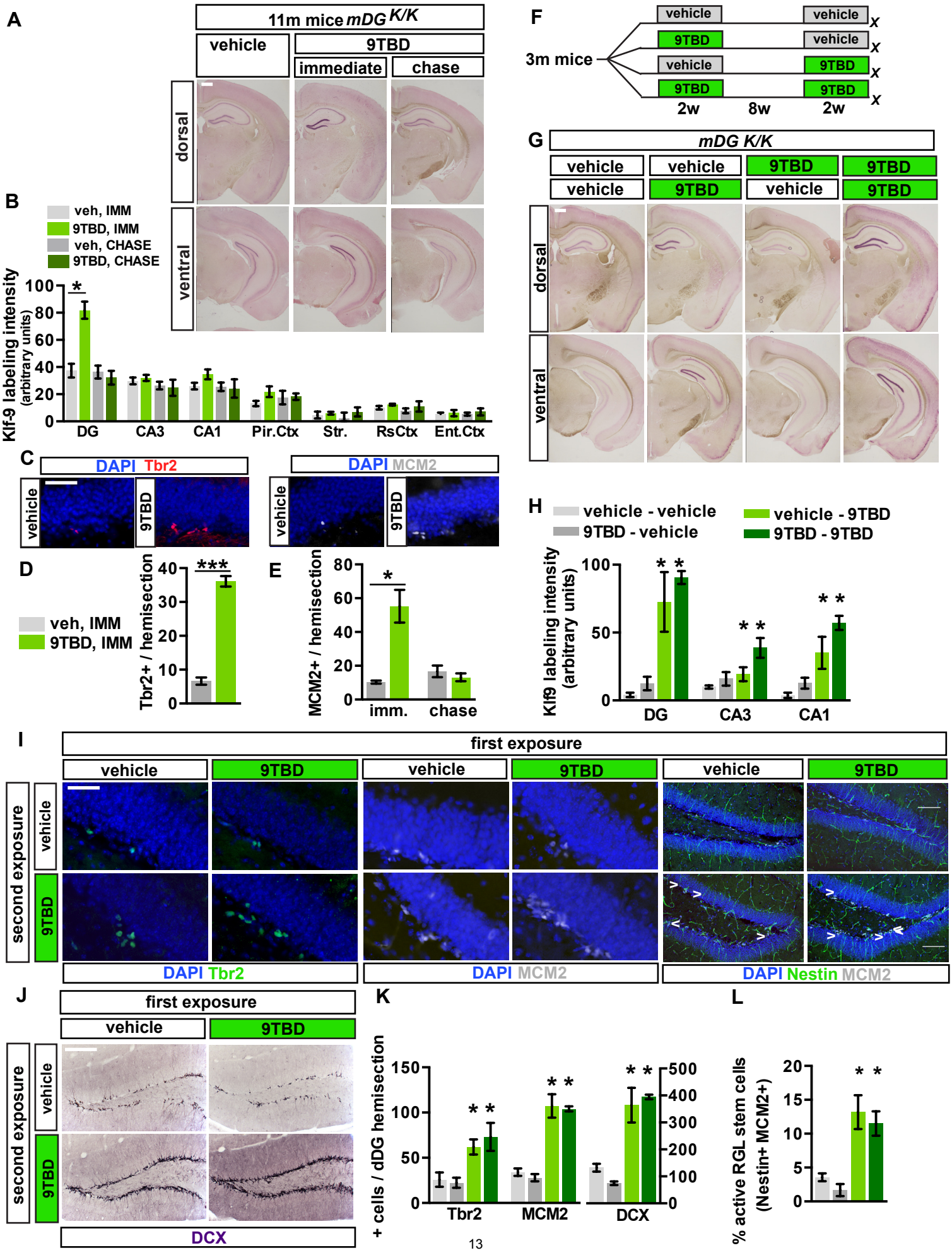
A
11m mice mDG K/K
vehicle
9TBD
immediate
chase
dorsal
ventral
B
veh, IMM
9TBD, IMM
veh, CHASE
9TBD, CHASE
Klf-9 labeling intensity (arbitrary units)
DG
CA3
CA1
Pir.Ctx
Str.
RsCtx
Ent.Ctx
C
DAPI Tbr2
DAPI MCM2
D
Tbr2+ / hemisection
E
MCM2+ / hemisection
imm.
chase
F
3m mice
2w
8w
2w
G
mDG K/K
H
vehicle - vehicle
9TBD - vehicle
vehicle - 9TBD
9TBD - 9TBD
Klf9 labeling intensity (arbitrary units)
I
first exposure
second exposure
DAPI Tbr2
DAPI MCM2
DAPI Nestin MCM2
J
DCX
K
+ cells / dDG hemisection
Tbr2
MCM2
DCX
L
% active RGL stem cells (Nestin+ MCM2+)

Supplementary Figure 7. Representative low magnification images of *c-fos* transcripts localized to nuclear, cytoplasmic, or both compartments in DGCs in response to same, similar or distinct contexts.
(Corresponds to Main Figure 8)

A) Representative confocal images of DG cells exhibiting cytoplasmic, nuclear or nuclear and cytoplasmic localization of *c-fos* transcripts. Scale bar: 50μm.

B) Genetic expansion of a cohort of 5-8 week-old adult-born DGCs decreases reactivation of DG cellular assemblies (A-A: n=6,4 A-B: n= 7,4 A-C: n=7,3, t-test, dorsal [vehicle: A-A vs. A-B p=0.8009, A-C p=0.0391], [9TBD: A-A vs. A-B p=0.0286, A-C p=0.1143]; ventral [vehicle: A-A vs. A-B p=0.2979, A-C p=0.0007]; [9TBD: A-A vs. A-B p=0.0017, A-C p=0.0055]). ***p<0.001, **p<0.01, *p<0.05. Bar graphs represent data as mean ± SEM.

Figure S7

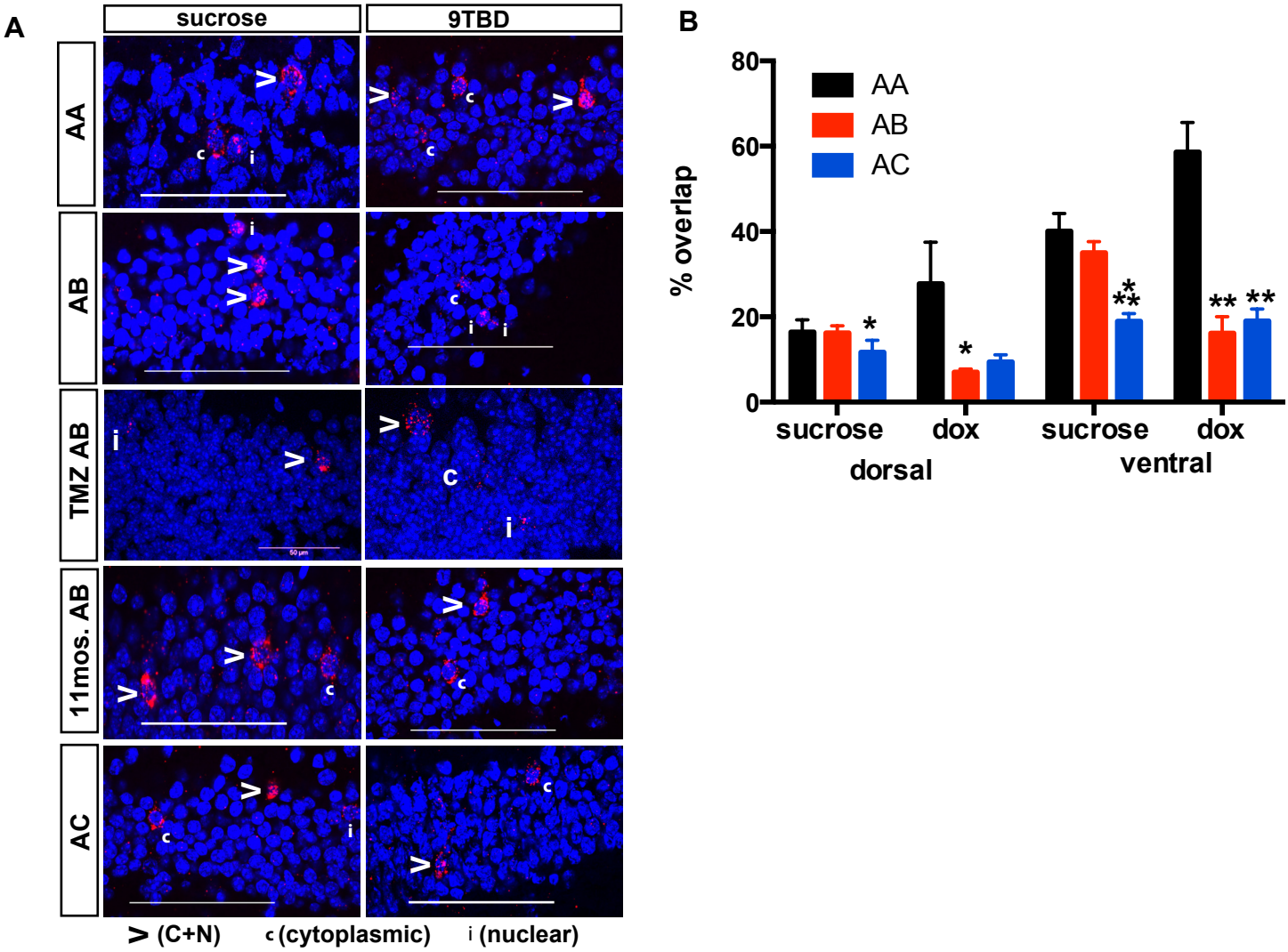
A
sucrose
9TBD
AA
AB
TMZ AB
11mos. AB
AC
> (C+N)
c (cytoplasmic)
i (nuclear)
B
% overlap
AA
AB
AC
sucrose
dox
sucrose
dox
dorsal
ventral

Detailed Methods

Generation of the teto-Klf9 mouse line:

A pGK Neo floxed STOP tetO cassette (Tanaka et al., 2010) was inserted upstream of the translation initiation site (ATG) of *Klf9* gene using standard bacterial artificial chromosome (BAC) recombineering techniques. Germ line-transmitted offspring were established as *Klf9 Floxed-STOP-tetO* heterozygous knock-in mice (Stop tetO Knock in allele, 8.9Kb band). *Floxed-STOP-tetO* mice were crossed with *ROSA-Flpe mice* (Farley et al., 2000) and FRT sites flanking the Neo-STOP cassette were recombined to generate *TRE-Klf9* knock in mice (tetO Knock in allele, 6Kb band). Southern Blotting was performed using a 5' probe at 5 kb upstream of the start site (Hind III digest) and a 3' probe 4.5 kb downstream of the start site (Nhe1 digest)(Figure 1A). 6 embryonic stem cells (129 SvEv ES cells, line CSL3) were identified to have undergone the desired gene targeting events. PCR genotyping was performed with a set of primers upstream of the insert and within the PGK Neo sequence, as well as a set of primers within the tetO sequence and downstream of the insert. Arrows in Figure 1A indicate location of primers used for genotyping.

Mouse lines:

The *teto-TauLacZ* reporter line has been described previously (Reijmers et al., 2007) and was purchased from Jackson labs (strain 008344; outcrossed from cfos-tTA). The *teto-Cre* line (Schonig et al., 2002) and inducible Beta galactosidase reporter line *(ROSA fSTOP lacZ)*(Soriano, 1999) have been described previously. The *teto-H2B-GFP* line was obtained from Dr. Konrad Hochedlinger (Foudi et al., 2009). The *teto-SynGFP; TdTomato* line was described previously (Li et al., 2010) and was purchased from Jackson labs (strain 012345). Nestin GFP mice were described previously (Mignone et al., 2004) and were obtained from Dr. David Scadden. *Thy1-GFP* (M Line) mice (Feng et al., 2000) were purchased from Jackson Labs (strain 007788) and were maintained by crossing with $^{K/K}$ or *mDG* $^{K/K}$ mice. *Rac1*$^{f/f}$ conditional mice were previously described (Glogauer et al., 2003) and were purchased from Jackson labs (strain 005550). Tail DNA from all offspring was genotyped by PCR to detect the presence of each transgene separately.

Temozolomide (TMZ) treatment

Briefly, TMZ (Sigma, T2577) was dissolved in DMSO at 25mg/ml, and diluted to 2.5mg/mL in sterile saline. Adult *mDG*$^{K/K}$ mice were given i.p. injections of saline +10% DMSO (vehicle) or TMZ on 3 consecutive days followed by four days with no injections for four weeks. At the start of the third week of dosing, animals were given BrdU via intraperitoneal injection, in 0.9% NaCl at 150mg/kg body weight. Mice did not show overt negative effects of the TMZ treatment and maintained body weight (±10% of starting weight).

Behavioral Experiments

Age-matched, genotyped-matched male *mDG* $^{K/K}$ mice (adult, 3-4 mos., middle-aged 12mos., aged, 17 mos.) were used for all behavioral experiments. Behavioral tasks were performed in the following order: open field (day 1), light-dark choice test (day 2), elevated plus maze (day 3), forced swim test (day 4,5). Novel object recognition, spatial learning and contextual fear conditioning were performed in separate cohorts. For the aged mice, open field and light-dark choice tests were performed prior to CFC. Mice were tested 4 weeks after 9TBD or vehicle treatment.

Open field

Mice were kept in a quiet, darkened room for at least 1 h before the test. Motor activity over 60 min was quantified in four Plexiglas open-field boxes of 41 x 41cm (Kinder Scientific) with 16 sets of double stacked pulse-modulated infrared photobeams equally spaced on every wall (128 total) to record *x–y* ambulatory movements. The software defined grid lines that divided each open field into center and surround regions, with the periphery consisting of the 10cm closest to the wall around the entire perimeter. Dependent measures were the distance traveled in the center, time spent in the center, and distance traveled in the center divided by total distance traveled (percentage distance). Overall motor activity was quantified as the total distance traveled (in centimeters).

Light–dark choice test

The light/dark test was conducted in the open-field chamber as above, but with a dark plastic box that is opaque to visible light but transparent to infrared covering one-half of the chamber area, thus creating dark and light compartments of equal size. An opening at floor level in the center of one wall of the dark compartment allowed passage between

the light and dark compartments. The light compartment was brightly illuminated. Mice were kept in a quiet, darkened room for at least 1 h before the test without food. Between each trial, the whole apparatus was cleaned. At the beginning of the test, the mouse was placed in the dark compartment and allowed to freely explore both compartments for 10 min. Ambulation distance and time spent in the dark and the light compartments were recorded.

Elevated Plus Maze test

The elevated plus maze consisted of black Plexiglass apparatus with four arms (16 cm long and 5 cm wide) set in a cross from a neutral central square (5 cm x 5 cm) placed 1m above the floor. Two opposing arms were delimited by vertical walls (closed arms), while the two other opposing arms had unprotected edges (open arms). Mice were placed in the center and their behavior was recorded for 5 min via a video camera system (ViewPoint, Lyon, France) located above the maze. Cumulative time spent in the open and closed arms, and entries into the open and closed arms, were scored manually by investigators blind to the treatment conditions. An arm visit was recorded when the mouse moved its forepaws into the arm.

Forced-swim test

Mice were placed in transparent plastic buckets (17 cm diameter; 25 cm deep) filled with 23-26°C water for 6 min and the animal's behavior was recorded using an automated video-tracking system. Testing was performed over 2 consecutive days with the first day serving the purpose of pre-exposure. Mobility (swimming and climbing behaviors) was analyzed using View-Point Life Sciences software.

Novel Object Recognition test

Mice were placed in an arena (45 cm long, 15 cm high and 30 cm wide) with two distinct objects for three sessions (7 minutes each), with a 3 minute intertrial interval. Mice became habituated to the objects during the three training sessions, and one of the objects was then replaced with a novel object in session four. Objects and object positions were counterbalanced during testing. The objects that were selected for testing elicited comparable levels of exploration based on exploration levels in pilot experiments. Sessions were videorecorded, and videos were manually scored for object

exploration (when an animal's snout was 2 cm or less from the object) by an investigator blind to object identity and animal treatment identity.

Contextual Fear conditioning

The contextual fear conditioning protocol (days 1-3) entailed delivery of a single 2 s footshock of 0.7 mA, 180 s after placement of the mouse in the training context. The mouse was taken out 20 s after termination of the footshock. Freezing levels were quantified over the initial 180s prior to the shock. On day 4, animals were exposed to with the training context (in which they did not receive a shock) or a similar context (designated B throughout) for three minutes. 14 and 28 days later, mice were exposed to the training and similar contexts in a counterbalanced design.

Conditioning was conducted in Coulbourn Habitest fear conditioning chambers. with clear front and back Plexiglas walls, aluminum side walls, and stainless-steel bars as a floor. The chamber was lit from above with a light, ventilated with a fan, and encased by a sound-dampening cubicle. On the days of testing, mice were brought out of the vivarium and allowed to habituate for an hour outside the testing room before starting the experiment. Mouse behavior was recorded by digital video cameras mounted above the conditioning chamber. For the training context (designated A throughout), the fan and lights were on, stainless-steel bars were exposed, and ethanol was used as an olfactory cue. Mice were brought into the testing room in a standard housing cage. For B, Mice were brought into the testing room in cardboard buckets. The similar context was modified by covering the stainless-steel bars with a solid floor covered with bedding, and two of the chamber walls were covered using plastic inserts with black and white shapes. Animals were counterbalanced for order of exposure, with the second exposure occurring 1h following the initial test. Exposure to the novel context (designated C throughout), occurred 1h following exposure to the second context. Mice were placed in individual round white cardboard paper chambers inside a large plastic enclosure. Freezeframe and Freezeview software (Actimetrics) were used for recording and analyzing freezing behavior, respectively.

Morris Water Maze and reversal learning

The task was performed with two training phases executed in succession: acquisition phase (9 days, Q3), and reversal phase (reversal learning, 5 days), with a hidden platform in the opposite quadrant (Q1). A probe trial, in which the mice were

released at the center of the opposite quadrent and were allowed to swim for 60 s in the absence of the platform, was performed 24h after the last trial of the acquisition phase (day 10) and twice during the reversal phase (day 13, prior to training, and day 16). The animals' trajectories were recorded with a videotracking system (AnyMaze). The apparatus consisted of a white pool 83cm in diameter and 60cm deep, filled with water to a depth of 29cm. Four black shapes were equally spaced on the walls of the tank as visible cues. Water temperature was maintained at approximately 25°C. A clear Plexiglas goal platform 5cm in diameter was positioned ~0.5cm below the surface of the water (hidden platform), approximately 15 cm from the wall of the tank. Latency to reach the platform and swim speed were recorded for training trials, while swim speed and time in quadrant were calculated for probe trials. Each trial comprised four tests, with mice released facing the wall in the center of each quadrant in a pseudorandom order such that no single start location was used in consecutive tests (10-min intertest interval). Mice were allowed to swim for 90s, and animals that failed to locate the platform in this time were guided to the platform and allowed to rest for 3s before being removed from the tank. 3 trials (~1h intertrial interval) were performed on days 1 - 9, and two trials per day on days 11-15. The average latency to reach the platform was averaged for each trial (4 tests) and for each day. A second cohort of mice (n=9 per group) was tested two weeks after local infusion of 9TBD or saline into CA1.

Cannula implantation and local infusion

Cannula implantation for drug delivery to CA1 was carried out as described previously (Goshen, Cell, 2011). Cannula were purchased from Plastics One (Roanoke, VA) and consisted of bilateral guide cannula (center to center 2.5mm, custom depth 1mm) and removable dummy cannula. Adult (12 - 16 week-old) *mDG* $^{K/K}$ mice were maintained under standard housing conditions, and anaesthetized with ketamine / xylazine (10mg/mL and 1.6mg/mL). Mice were placed in the stereotaxic apparatus and small hole was drilled at each bilateral injection location (anterioposterior = -2mm from bregma; lateral = ±1.25mm) and cannula slowly lowered to the appropriate depth. The cannula was secured to the skull with dental cement. After allowing one week for the mice to recover, the dummy cannula was removed, and the injection cannula was inserted through the guide cannula, from which it projected 0.5mm. The injection cannula was attached to PE50 tubing and a New Era Syringe pump. Saline or 9TBD (dose 10mg /mL, 10µg infused in 1µl) was infused at a rate of 1µl / minute on each side sequentially to

ensure equal delivery. Drug or vehicle was infused every other day for 10 days (5 injections).

Retroviral / Rabies virus / AAV injections

For all surgeries, mice were given carbofen (5mg/kg body weight subcutaneous in sterile saline) prior to surgery and 24h later to minimize discomfort.

Retroviral infection: Briefly, stable human 293-derived gpg retroviral packaging cell line (kindly provided by S. Ge, Stony Brook University School of Medicine, NY) was co-transfected with retroviral plasmids expressing TdTomato (generous gift of Dr. Shaoyu Ge) and pVSVG. Virus-containing supernatant was harvested 36, 48, and 60 h after transfection and concentrated by ultracentrifugation at 25,000 rpm for 1.5 h. Adult (6 - 8 week- old) *mDG* $^{K/K}$ mice and $^{K/K}$ littermates were maintained under standard housing conditions, and anaesthetized with ketamine / xylazine (10mg/mL and 1.6mg/mL). Mice were placed in the stereotaxic apparatus and small hole was drilled at each bilateral injection location and injected with 1µl virus per site injected using a Hamilton microsyringe (0.1 µl/min) into the dorsal DG using the following coordinates: anterioposterior = −2 mm from bregma; lateral = ± 1.6 mm; ventral = 2.5 mm. The skin incision was closed carefully after retroviral injection to minimize inflammation. Injection needles were left in place for 10 min after injection to ensure even distribution of the virus. Mice were sacrificed 5 weeks post infection to examine mossy fiber terminal (MFT) connectivity of TdTomato+ adult-born neurons. (See Figure S4C for timeline.)

Rabies virus: The retrovirus CAG-DsRedExpress2-2A-G-IRES2-TVA, encoding DsRedExpress2, the RABV glycoprotein (G), and TVA800 (the GPI anchored form of the TVA receptor), designed as retro-DsRed-G-TVA, was described previously (Deshpande et al., 2013, Begami, 2015). This plasmid was used to transfect the 293-derived gpg retroviral packaging cell line as described above, except virus was harvested at 2, 4, and 6 days after transfection, followed by ultracentrifugation to concentrate the virus. Construction and amplification of the G gene-deleted GFP-expressing RABV (SADDG-GFP, here designated RABVΔG) have been described previously (Wickersham et al., 2007a; Wickersham et al., 2007b; Bergami et al., 2015). Bilateral dorsal DG stereotaxic injections of retro-DsRed-G-TVA in *mDG* $^{K/K}$ mice were carried out as described above. Psuedotyped rabies virus was injected at the same stereotaxic coordinates, three or five weeks following starter virus retroviral infection. For the 4 week cohort, mice were treated with vehicle or 9TBD for 14 days starting at 3 days post-retroviral injection,

injected with RABVΔG four days after the end of treatment, and sacrificed 1 week later (to allow expression and propagation of RABVΔG). For the 6 week cohort, mice were treated with vehicle or 9TBD for 14 days starting at 1 week post-retroviral injection, injected with RABVΔG 2 weeks after the end of treatment, and sacrificed 1 week later (See timeline in Figure 5E). Connectivity ratios were computed as (traced cells, GFP+)/ (starter cells, GFP+DsRed+).

AAV: For injection analysis of dendritic spine density in striatum and retrosplenial cortex, AAV_9-CaMKinaseIIα-GFP virus was purchased from the University of Pennsylvania virus core (titre $6.27x10^{13}$). Virus was diluted 1:50 to allow sparse infection, and 0.1 µl (0.05 µl/min) injected in the striatum (anterioposterior = +1mm from bregma; lateral = -1.9mm; ventral = -3.2 mm from skull surface) and retrosplenial cortex (anterioposterior = -1.6mm from bregma; lateral = ±0.5mm; ventral = -1.3mm from skull surface) using the anaesthetization protocol described above. Mice were treated with vehicle or 9TBD for 14 days starting at 3 days post-surgery, and sacrificed 2 weeks following the end of treatment.

Rac1: Viruses were diluted (below) to ensure local infection of the Cre virus and very sparse labeling with eYFP to facilitate spine analysis. To control for virus, floxed/floxed and wildtype littermates were injected with Cre/ DIO eYFP viruses (1:100 CRE + 1:500 DIO-eYFP). (University of Pennsylvania virus core, Cre titre $1.07x10^{13}$, University of North Carolina virus core, DIO-eYFP titre $5.87x10^{12}$). To control for genotype, floxed/floxed mice were injected with AAV_9-CaMKinaseIIα-GFP virus + AAV_5-EF1α–DIO-eYFP (1:50 DIO-eYFP + 1:1000 GFP) viruses (University of Pennsylvania virus core, GFP titre $6.27x10^{13}$). Equal total viral particles were injected for each group. 0.2µl (0.05 µl/min) of virus cocktail was injected in the molecular layer of the DG (from bregma: anterioposterior = -2mm; lateral = +1.4mm; ventral = -2.1mm from skull surface) using the anaesthetization protocol described above.

Sholl analysis of 4 and 6-week-old neurons

A Nikon A1R Si confocal laser, a TiE inverted research microscope, and NIS Elements software were used to capture z-stacks for Scholl analysis using a 20x objective. Images were acquired as 30 µM Zstacks with a step size of 2.5 µM. Images of collapsed z-stacks were analyzed for total length using the tracing tool in NIS Elements. Dendritic complexity was analysed using the Sholl analysis tool in NIS Elements. The centre of all concentric circles was placed at the centre of the cell's soma. The parameters used

were starting radius (30 μm), ending radius (250 μm from the centre) and interval between consecutive radii (30 μm). Total branch number was counted manually, as were the number of branch intersections at each distance from the soma by an investigator blind to experimental conditions.

Image analysis of mossy fiber terminals

A Nikon A1R Si confocal laser, a TiE inverted research microscope, and NIS Elements software were used to capture z-stacks for Mossy fiber terminal (MFT) imaging using a 60x objective as we recently published (Ikrar et al., 2013). Images were acquired as 15 μM Zstacks with a step size of 0.5 μM. Area of individual MFTs was assessed at the widest point in the Z-stack using Image J MaxEntropy thresholding, followed by unbiased area selection with the tracing tool. MFTs area was analysed for >50 individual MFTs per mouse (702 total) to calculate the cumulative percentage of terminals at each size or smaller.

Image analysis of dendritic spines

For quantification of dendritic spines, confocal z-stack images were acquired using a Nikon A1R Si confocal laser, a TiE inverted research microscope, and NIS Elements software. Imaging was performed using a 60x objective, plus 1.5x optical zoom and 6x digital zoom. For spine imaging, confocal 2.1uM z-stacks (2048 resolution) with 0.3uM step size were taken centered on dendritic segment. Z-stacks were flattened using the maximum intensity projection, and flattened images were quantified using image J. For spine density, spines were counted manually for at least 80uM of dendritic length per region per mouse. The Edge fitter plugin (www.ghoshlab.org) was used to measure head diameter (at the widest point of the spine head) while length was measured manually from dendrite to the furthest point of the spine head. >150 spines were analyzed per region per mouse to calculate spine size distribution (4,538 DG and 5,138 CA1 spines from 14 mice). The outer molecular layer was defined as the 1/3 of the molecular layer furthest from the granule cell layer, while the inner molecular layer was defined as the 1/3 of the dendritic tree closest to the granule cell layer. Stratum radiatum was defined as the 2/3 of the dendritic tree ventral to the pyramidal layer. For quantification of spines containing PSD95, confocal 2.1μm z-stacks (2048 resolution) with 0.3μm step size were taken centered on dendritic segment. Spines were considered

positive for PSD95 if PSD95 labeling overlapped with the GFP+ spine head in any plane. All imaging and quantification were performed by an investigator blind to treatment.

Immunohistochemistry and quantification

Sections were stored in PBS with 0.01% sodium azide at 4°C. For BrdU, CldU/ IdU, CldU/ GFP, MCM2, MCM2/ GFP, MCM2/ Nestin/ Tbr2, and BrdU / GFAP / NeuN immunohistochemistry, sections (1 set) were mounted onto SuperFrost Plus charged glass slides. Sections were subjected to antigen retrieval in 10 mM citrate buffer (pH 6) using a boiling protocol. After cooling to room temperature, sections were rinsed three times in PBS and blocked in PBS with 0.3% Triton X-100 and 10% normal donkey serum (NDS) for 2 h at room temperature. Incubation with primary antibodies (rat anti-BrdU 1:100 dilution, Serotec; mouse anti-MCM2 1:500, BD Biosciences; chicken anti-Nestin 1:500, Aves; rabbit anti-Tbr2, 1:500, Abcam; mouse anti-NeuN 1:500, Chemicon; Rabbit anti-GFAP, 1:1000 DAKO) was carried out at 4°C overnight. Fluorescent-label-coupled secondary antibodies (Jackson ImmunoResearch) were used at a final concentration of 1:300 in PBS:glycerol.

For assessment of neuronal age in *mDG* $^{K/+;\ teto\ H2BGFP/+}$ mice injected with CldU/IdU, antigen retrieval was carried as described for BrdU labeling above. Rat ant-BrdU (Accurate Chemicals, 1:500, recognizes CldU but not IdU) and mouse anti-BrdU (BD Biosciences, 1:50, recognizes IdU but not CldU) were used as described previously (Stone et al., 2011) along with anti-GFP (rabbit, 1:1000, Life Technologies). 303 XdU+ cells were analyzed for three mice. For assessment of neuronal age in *mDG* $^{K/+;\ teto\ H2BGFP/+}$ mice, *mDG* $^{K/+;\ teto\ TauLacZ/+}$ mice, and *mDG* $^{K/+;\ tetoTdTomato/+}$ mice, floating sections were labeled for GFP (rabbit, 1:1000, Life Technologies and DCX (Santa Cruz, goat, 1:500), β-galactosidease (chicken, 1:1000, Abcam) and DCX, or DsRed (rabbit, 1:1000, Clontech) and DCX respectively using the same protocol as used for cfos. 2320 cells were counted from 9 mice of three genotypes. To assess the age of GFP expressing cells in *mDG*$^{K/K;Thy\text{-}1GFP}$ mice, CldU and GFP labeling was carried out as described for BrdU. 187 cells were counted from three mice.

To assess stem cell activation, sections from *mDG* $^{K/K}$ mice were double-labeled for Nestin and MCM2 as described above. In addition, sections from *mDG* $^{K/K;\ Nestin\ GFP+}$ mice were double-labeled for GFP and MCM2 as described above. Confocal stacks (1024 resolution, 2μm step size, 24 μm z-stack) were taken through 3-6 dorsal DG hemisections per mouse. Activated stem cells were defined as Nestin+ cells (or GFP+

cells) with radial glial-like morphology that showed colocalization of MCM2. Nestin+MCM2+ (or GFP+ MCM2+) were counted and quantified as a percentage of the total Nestin+ (or GFP+) population with radial glial-like morphology.

For DCX immunohistochemistry, floating sections were first quenched to remove endogenous peroxidase activity (with 1% H2O2 in 1:1 PBS:methanol). Sections were then washed in PBS, blocked (in PBS containing 0.3% Triton X-100 and 10% NDS) and incubated with primary antibody overnight at 4 °C (DCX, goat, 1:2000, SantaCruz Biotechnology). Following washes in PBS, sections were incubated with horse-radish-peroxidase-coupled, biotinylated secondary antibodies for 2h. Following incubation with ABC solution (Vector Labs) for 1h, the color reaction was carried out using a DAB kit (Vector Labs). X-Gal staining for ß-galactosidase activity was performed as previously described (Schonig et al., 2002)

For BrdU, Tbr2, MCM2, and DCX analysis, positive cells in the granule cell layer and sub-granule zone were counted manually along the dorsal to ventral axis of the DG (1 set of 6; 9 sections). Summing the counted cells and multiplying by 6 yields the total per animal. For c-fos analysis, positive cells in the granule cell layer and CA3 or CA1 pyramidal layer were counted manually along the dorsal to ventral axis of the hippocampus (1 set of 6; 3 sections each dorsal, intermediate, and ventral regions).

For assessing neurogenesis in the SVZ, matched sections were compared throughout the dorsal to ventral extent of the SVZ according to the Paxinos and Franklin atlas. DCX positive cells at the border of the ventricular zone were counted manually per hemisection. In a separate cohort of mice, proliferation in the SVZ was assessed by counting SVZ BrdU positive cells (2 hours post-injection of BrdU). Survival of SVZ generated neurons was assessed by counting BrdU-positive neurons in the granule layer in the MOB.

To label c-fos (rabbit, Calbiochem, 1:10,000) and Cleaved caspase-3 (Cell Signaling, rabbit, 1:500) floating sections were used. Briefly, sections were washed in PBS, blocked in PBS buffer containing 0.3% Triton X-100 and 10% NDS, and incubated in primary antibodies overnight with shaking at 4 °C. The next day, sections were washed three times in PBS and incubated with fluorescent-label-coupled secondary antibodies (Jackson ImmunoResearch) for 2 h at room temperature. Data shown as cells per hemisection. For PSD95 / GFP / VGlut1 labeling, sections were labeled as for c-fos, except PBS with 0.5% Triton X-100 was used in place of the 0.3% Triton X-100. The PSD95 antibody was developed by / obtained from the UC Davis/ NIH NeuroMab

Facility (clone K28/43 mouse, 1:500). Primary antibodies VGlut-1 (Synaptic Systems, guinea pig, 1:2000), GFP (Novus, goat, 1:500).

All analysis was performed by an investigator blinded to treatment and/or genotype. Dorsal and ventral sections were defined according to the Paxinos and Franklin (1997) atlas (dorsal Bregma -0.9mm to -2.1mm ; ventral Bregma -2.7mm to -3.88mm).

In situ hybridization

In situ hybridization (ISH) was performed using dioxygenin-labeled riboprobes on 35µm cryosections generated from perfused tissue as described previously (Scobie et al., 2009). Premixed RNA labeling nucleotide mixes containing digoxigenin-labled UTP (Roche Molecular Biochemicals) were used to generate RNA riboprobes. Riboprobes were purified on G-50 Microspin columns (GE Healthcare). Probe concentration was confirmed by Nanodrop prior to the addition of formamide. Briefly, sections were mounted on charged glass (Superfrost Plus) slides and postfixed for in 4% paraformaldehyde (PFA). Sections were then washed in DEPC-treated PBS, treated with proteinase K (40 µg/ml final), washed again in DEPC-treated PBS, and then acetylated. Following prehybridization, sections were incubated with riboprobe overnight at 58°, washed in decreasing concentrations of SSC buffer, and immunological detection was carried out with anti-Dioxygenin antibody conjugated with alkaline phosphatase (Roche). Color reaction was carried out with NBT/BCIP. Color reaction times were identical for both treatment groups. For quantification, 2-4 color images per region per mouse were analyzed using the mean intensity function in Image J. All images were captured using the same light intensity and exposure times. The mean intensity of the region of interest (minus mean intensity of a selected background region) was averaged across images for each mouse and each treatment group.

catFISH: Riboprobes were prepared as for Klf9. Coronal brain sections (20 µm) were prepared using a cryostat and representative series of dorsal and ventral hippocampal sections were organized on slides (Superfrost Plus, VWR) and stored at –80°C until use. Sections were fixed in 4% buffered paraformaldehyde, treated with 0.5% acetic anhydride/1.5% triethanolamine, and incubated in acetone:methanol, equilibrated in 2xSSC before equilibration in prehybridization solution for 1h. Riboprobes were diluted to (2.5ng /µl; 150 µl per slide) in hybridization buffer, heat denatured, chilled on ice, and then added to each slide. Coverslips were added to the slides, and hybridization was

carried out at 65°C for 16 hours. Slides were washed in decreasing concentrations of SSC, including a wash at 37°C in 2x SSC with RNase A (10 µg per ml), and a final wash in 0.5xSSC at 55°C. Endogenous peroxidase activity was quenched with 2% H202 in SSC, slides were blocked (with blocking agent from the DirectFISH kit [NEN Life Sciences, Boston, Massachusetts] plus 5% sheep serum and 0.1% Tween-20), and incubated with horseradish peroxidase (HRP)-antibody conjugate (0.16 µg per ml; Jackson Immunoresearch) overnight at 4°C. Slides were washed three times in Tris-buffered saline (with 0.05% Tween-20), and then a 1:50 dilution of the CY3-tyramine substrate (Perkin Elmer) was added for 30m at RT. Slides were washed three times in Tris-buffered saline (with 0.05% Tween-20) and coverslipped with mounting media containing DAPI (Fluoromount with DAPI, Southern Biotech). Confocal z-stack images using a 60x objective (0.75 µm step size) were acquired along the DG GCL using a Nikon A1R Si confocal laser, a TiE inverted research microscope, and NIS Elements software. Image analysis was performed with NIS Elements software. Four to eight hemisections were scanned per mouse. Images were manually counted for *c-fos* labeling. For analysis of global remapping using catFISH, the exposure paradigms utilized the training context associated with a foot-shock (context A) and exposure to a similar context (high interference, context B), or distinct context (low interference, context C), or re-exposure to the training context. Quantification was performed by an investigator blind to treatment condition.

Statistical Analysis

Statistical analysis was carried out using GraphPad Prism software. Unpaired two-tailed Student's t-tests were used to compare two groups. In the text and figure legends, "n" indicates number of mice per group. Further details of quantification are under each methods section. *, $P<0.05$. To compare groups across training days for the morris water maze and contextual fear conditioning, two-way repeated measures ANOVA was used. For the morris water maze probe test analysis, one-way ANOVA was performed for each group to compare preference for each quadrant. For contextual fear conditioning, behavioral data were scored by two experimenters, including one unrelated to the project. Spine head diameter distribution and mossy fiber terminal size distribution were assessed using Komolgrov-Smirnov tests with significance at $p<0.001$. Spearman's rank-order correlation analysis was performed to analyze the relationship between spine density and DCX+ population.

Supplementary References

Bergami, M., Masserdotti, G., Temprana, S.G., Motori, E., Eriksson, T.M., Gobel, J., Yang, S.M., Conzelmann, K.K., Schinder, A.F., Gotz, M.*, et al.* (2015). A critical period for experience-dependent remodeling of adult-born neuron connectivity. Neuron *85*, 710-717.

Farley, F.W., Soriano, P., Steffen, L.S., and Dymecki, S.M. (2000). Widespread recombinase expression using FLPeR (flipper) mice. Genesis *28*, 106-110.

Feng, G., Mellor, R.H., Bernstein, M., Keller-Peck, C., Nguyen, Q.T., Wallace, M., Nerbonne, J.M., Lichtman, J.W., and Sanes, J.R. (2000). Imaging neuronal subsets in transgenic mice expressing multiple spectral variants of GFP. Neuron *28*, 41-51.

Foudi, A., Hochedlinger, K., Van Buren, D., Schindler, J.W., Jaenisch, R., Carey, V., and Hock, H. (2009). Analysis of histone 2B-GFP retention reveals slowly cycling hematopoietic stem cells. Nature biotechnology *27*, 84-90.

Glogauer, M., Marchal, C.C., Zhu, F., Worku, A., Clausen, B.E., Foerster, I., Marks, P., Downey, G.P., Dinauer, M., and Kwiatkowski, D.J. (2003). Rac1 deletion in mouse neutrophils has selective effects on neutrophil functions. J Immunol *170*, 5652-5657.

Ikrar, T., Guo, N., He, K., Besnard, A., Levinson, S., Hill, A., Lee, H.K., Hen, R., Xu, X., and Sahay, A. (2013). Adult neurogenesis modifies excitability of the dentate gyrus. Frontiers in neural circuits *7*, 204.

Li, L., Tasic, B., Micheva, K.D., Ivanov, V.M., Spletter, M.L., Smith, S.J., and Luo, L. (2010). Visualizing the distribution of synapses from individual neurons in the mouse brain. PLoS ONE *5*, e11503.

Mignone, J.L., Kukekov, V., Chiang, A.S., Steindler, D., and Enikolopov, G. (2004). Neural stem and progenitor cells in nestin-GFP transgenic mice. J Comp Neurol *469*, 311-324.

Reijmers, L.G., Perkins, B.L., Matsuo, N., and Mayford, M. (2007). Localization of a stable neural correlate of associative memory. Science *317*, 1230-1233.

Schonig, K., Schwenk, F., Rajewsky, K., and Bujard, H. (2002). Stringent doxycycline dependent control of CRE recombinase in vivo. Nucleic Acids Res *30*, e134.

Scobie, K.N., Hall, B.J., Wilke, S.A., Klemenhagen, K.C., Fujii-Kuriyama, Y., Ghosh, A., Hen, R., and Sahay, A. (2009). Kruppel-like factor 9 is necessary for late-phase neuronal maturation in the developing dentate gyrus and during adult hippocampal neurogenesis. J Neurosci *29*, 9875-9887.

Soriano, P. (1999). Generalized lacZ expression with the ROSA26 Cre reporter strain. Nat Genet *21*, 70-71.

Stone, S.S., Teixeira, C.M., Zaslavsky, K., Wheeler, A.L., Martinez-Canabal, A., Wang, A.H., Sakaguchi, M., Lozano, A.M., and Frankland, P.W. (2011). Functional convergence of developmentally and adult-generated granule cells in dentate gyrus circuits supporting hippocampus-dependent memory. Hippocampus *21*, 1348-1362.

Tanaka, K.F., Ahmari, S.E., Leonardo, E.D., Richardson-Jones, J.W., Budreck, E.C., Scheiffele, P., Sugio, S., Inamura, N., Ikenaka, K., and Hen, R. (2010). Flexible Accelerated STOP Tetracycline Operator-knockin (FAST): a versatile and efficient new gene modulating system. Biol Psychiatry *67*, 770-773.

Wickersham, I.R., Finke, S., Conzelmann, K.K., and Callaway, E.M. (2007a). Retrograde neuronal tracing with a deletion-mutant rabies virus. Nature methods *4*, 47-49.

Wickersham, I.R., Lyon, D.C., Barnard, R.J., Mori, T., Finke, S., Conzelmann, K.K., Young, J.A., and Callaway, E.M. (2007b). Monosynaptic restriction of transsynaptic tracing from single, genetically targeted neurons. Neuron *53*, 639-647.